The Eagle Nebula's fingers - pointers to the earliest stages of star formation?

Journal Item

Astron. Astrophys. 342, 233–256 (1999)

ASTRONOMY AND ASTROPHYSICS

The Eagle Nebula's fingers – pointers to the earliest stages of star formation?

G.J. White[1], R.P. Nelson[2], W.S. Holland[3], E.I. Robson[3], J.S. Greaves[3], M.J. McCaughrean[4], G.L. Pilbratt[5], D.S. Balser[6], T. Oka[7], S. Sakamoto[8], T. Hasegawa[9], W.H. McCutcheon[10], H.E. Matthews[3], C.V.M. Fridlund[5], N.F.H. Tothill[1], M. Huldtgren[11], and J.R. Deane[1]

[1] Department of Physics, Queen Mary and Westfield College, University of London, Mile End Road, London E1 4NS, UK
[2] Astronomy Unit, Queen Mary and Westfield College, University of London, Mile End Road, London E1 4NS, UK
[3] Joint Astronomy Centre, 660 N A'ōhōku Place, University Park, Hilo, Hawaii 96720, USA
[4] Astrophysikalisches Institut Potsdam, An der Sternwarte 16, D-14482 Potsdam, Germany
[5] ESA Astrophysics Division, Space Science Department, ESTEC, P.O.Box 299, 2200 AG Noordwijk, The Netherlands
[6] NRAO, P.O. Box 2, Green Bank, WV 24944, USA
[7] Cosmic Radiation Laboratory, RIKEN, 2-1 Hirosawa, Saitama 351-01, Japan
[8] Nobeyama Radio Observatory, Nobeyama, Minamisaku, Nagano 384-13, Japan
[9] Institute of Astronomy, University of Tokyo, 2-21-1 Osawa, Mitaka, Tokyo 181, Japan
[10] University of British Columbia, Physics Department, Vancouver, BC V6T 2A6, Canada
[11] Stockholm Observatory, SE-13336 Saltsjobaden, Sweden

Received 24 June 1998 / Accepted 16 October 1998

Abstract. Molecular line, millimetre/submillimetre continuum, and mid-IR observations are reported of the opaque fingers which cross the Eagle Nebula. The fingers are surprisingly warm when viewed in the CO *J*= 3–2 lines, with kinetic temperatures approaching 60 K, although the lines are relatively narrow. Most of the mass in the fingers is concentrated in cores which lie at the tips of the fingers, and contain from ~ 10 to 60 $M_\odot$, representing 55–80% of the mass of the individual fingers. The integrated mass contained in the three fingers and the nearby extended material is ~ 200 $M_\odot$. The velocity fields of the gas are complex and the material is very clumpy. The best evidence for coherent velocity structure is seen running along the central finger, which has a velocity gradient $\sim 1.7\,\mathrm{km\,s^{-1}\,pc^{-1}}$. The fingers contain several embedded submm continuum cores, with the most intense located at the tips of the fingers. The continuum spectra of these cores shows that they are much cooler, $T_{dust} \sim 20$ K, than $T_{gas} \sim 60$ K of their respective fingers. A simple thermal and chemical model of a finger was developed to study the physical environment, which takes into account the external UV illumination ($\sim 1700\ G_0$), and the chemical and thermal structure of a finger.

The model predictions are consistent with all of the available observations. The fingers appear to have been formed after primordial dense clumps in the original cloud were irradiated by the light of its OB stars. These clumps then shielded material lying behind from the photoevaporative dispersal of the cloud, and facilitated the formation of the finger structures. The cores in the tips of the fingers appear to be at a very early stage of *pre-protostellar* development: there are no embedded infrared sources or molecular outflows present. The pressure inside the cores is just less than that of the surrounding gas, allowing them to be compressed by the external pressure. The cores are probably just starting the final stages of collapse, which will lead to the formation of a condensed, warm object. It is well known that such characteristics are expected from the earliest stages of objects popularly known as 'protostars'. *The cores in the tips of the Eagle Nebula's fingers have characteristics similar to those expected to occur in the earliest stages of protostellar formation.*

Key words: infrared: ISM: continuum – ISM: molecules – ISM: individual objects: Eagle Nebula – ISM: H II regions – ISM: general ISM: clouds

1. Introduction

The Eagle Nebula, M16, is a prominent HII region lying 2 ± 0.1 kpc from the Earth (Hillenbrand et al.1993). Optical images show it to be crossed by several opaque 'Elephant Trunks', which appear as 'fingers', or columns of dense obscuring material projected against the diffuse background nebular emission. The Eagle Nebula lies adjacent to the star cluster NGC6611, which contains the largest population of intermediate-mass pre-main-sequence stars known in any young cluster in the Galaxy (Hillenbrand et al. 1993). It is made up of several hundred optically visible stars whose masses lie in the range $3 < M < 8$ $M_\odot$, and ages range from ~ 0.25 to $3\ 10^6$ years. While most of the stars in this cluster seem to have formed in a mini-starburst $\sim 2\ 10^6$ years ago, high-mass star-formation has been occurring over at least the last $6\ 10^6$ years (Hillenbrand et al. 1993). A recent study with the Hubble Space Telescope (HST – Hester et al. 1996) discovered a population of seventy-three 'evaporating

Send offprint requests to: g.j.white@qmw.ac.uk

Table 1. JCMT telescope parameters – April 1996

Line	Transition	Freq GHz	T_{sys} K	HPBW $''$	$\eta_{\rm fss}$	$\eta_{\rm mb}$	Spectra	rms K
HCN	1–0	86.630	310	44	0.70	0.64	4	0.2
HCO^+	1–0	86.754	350	44	0.70	0.64	4	0.2
$H^{13}CO^+$	1–0	89.188	240	43	0.65	0.64	4	0.2
CS	2–1	97.981	240	43	0.65	0.64	4	0.2
$C^{18}O$	1–0	109.782	370	35	0.65	0.48	4	0.2
^{13}CO	1–0	110.201	420	34	0.6	0.48	4	0.2
CO	1–0	115.271	1700	33	0.6	0.47	4	0.2
$C^{18}O$	2–1	219.560	350	22	0.80	0.64	4	0.2
CO	2–1	230.538	330	21	0.80	0.64	4	0.2
$C^{18}O$	3–2	329.331	500	16	0.75	0.65	563	1.2
^{13}CO	3–2	330.588	500	16	0.75	0.65	120	1.5
CO	3–2	345.796	360	15	0.75	0.65	1410	0.5
HCO^+	4–3	356.734	430	14	0.75	0.65	457	0.6
CI	$^3P_1$–$^3P_0$	492.161	3000	10	0.7	0.53	504	3.0

gaseous globules' (EGG's). About 7% of these have associated young stars, although it was speculated that a more complete survey capable of tracing a lower mass embedded population would find that as many as $\sim$ 20% of the EGG's might contain young stars (McCaughrean 1997).

The radiation from several of the nearby O-stars has photoevaporated much of the material in the original molecular cloud, and the fingers may mark the location of dense clumps which existed in the primordial molecular cloud from which NGC6611 was formed. These dense clumps would then have shielded the material lying behind them from the photoevaporative effects of the UV radiation, leading to the formation of the fingers (similar to the way that 'capstones' can effect the geological erosion of material on the earth). The surface layers of these fingers are ionised by the UV radiation emitted by several O5 stars lying about 2 pc to the NW, which provide a total flux of $\sim 2\ 10^{50}$ photons s^{-1} (Hester et al. 1996). The material *inside* the surface layers must therefore be subjected to the pressure of the surrounding hot ionised gas, although the state of dynamical equilibrium will also depend on the internal pressure, magnetic field strengths and the gravitational stability of the cores.

The optical appearance of the fingers therefore suggests that the dense, opaque material near the tips of the fingers may have shielded the material lying behind from the effects of the radiation, and that this shielding may have contributed to the formation of the fingers. This paper will examine a) the structure and properties of the gas and dust in the fingers, b) the thermal and pressure equilibrium of the cores and fingers, and c) the prospects for future star formation and the subsequent evolution of the fingers. For brevity, we adopt a naming convention designating the three fingers, running from north to south as $\mathbf{\Pi_1}$, $\mathbf{\Pi_2}$, and $\mathbf{\Pi_3}$, respectively.

2. The observations

Spectral line and continuum observations of an area covering the three main fingers at millimetre and sub-millimetre wavelengths, were made with the 15 metre James Clerk Maxwell Telescope (JCMT) in Hawaii during April and September 1997. These were supplemented by millimetre wavelength spectroscopic observations using the Onsala Space Observatory (OSO) 20 metre telescope during March 1998. The telescope efficiencies and beamsizes at the various frequencies are summarised in Table 1 (observations below 116 GHz were made at OSO, those above 200 GHz at the JCMT):

The spectral data were collected during periods of good atmospheric transparency, when both the JCMT and OSO's pointing and tracking accuracy were better than $2''$. The JCMT spectra were collected and processed using standard JCMT receivers with a digital autocorrelation spectrometer backend. The receivers had single sideband system noise temperatures ranging from 300 K in the CO *J*= 2-1 and 3–2 transitions, 400 K for HCO^+ *J*= 4–3 to 3000 K for the CI measurements, and the data were taken with velocity resolutions of ~ 0.2 km s^{-1}. The OSO spectra were observed using a frequency switching with an SIS receiver which was operated in a single-sideband mode. This was used with a digital autocorrelation receiver, which provided a spectral resolution ~ 0.06 km s^{-1}. The data were calibrated in units of main beam brightness temperature T_{mb} (= T_a*/η_{mb}) using a standard chopper wheel calibration technique with an additional correction for the relative sideband gains, and an η_{mb} value measured from observations of the planets. The T_{mb} scale describes the brightness of a source which completely fills the main beam, but is not seen by the side-lobes. The maps presented later indicate that this is generally the case in the *J*= 3–2 observations.

Several 'Standard' calibration line sources were observed over a range of elevations at both OSO and the JCMT, and their intensities found to be in good agreement with historical values. In particular the Eagle Nebula was observed at low elevations from Onsala (maximum elevation 18 degrees). Frequent observations of compact standard calibration sources observed at low elevations agreed to within 10 percent of values obtained

Table 2. Photometry at the submm peaks (all fluxes in Janskys per beam, position offsets are in $''$).

μm	(-20,+30)	(-45,-28)	(-45,-75)	(20,-30)	(95, -205)
2000	0.276 ± 0.023	0.140 ± 0.013	0.088 ± 0.013	0.097 ± 0.016	0.149 ± 0.016
1350	0.475 ± 0.032	0.294 ± 0.026	0.143 ± 0.015	0.168 ± 0.018	0.288 ± 0.026
850	1.24 ± 0.01	0.785 ± 0.019	0.34 ± 0.02	0.434 ± 0.023	0.884 ± 0.033
750	1.46 ± 0.03	1.19 ± 0.07	0.464 ± 0.062	0.584 ± 0.051	1.19 ± 0.09
450	6.0 ± 0.22	3.77 ± 0.25	1.49 ± 0.23	2.20 ± 0.15	3.63 ± 0.28
350	11.4 ± 0.23	8.08 ± 0.20	2.26 ± 0.18	2.98 ± 0.3	5.01 ± 0.17

at higher elevations. At the JCMT, each of the map grids were sampled every $6''$ - except the CI map, which was sampled every $4''$. All of the JCMT spectral line data were position switched against a clean off-position 0.8 degrees NW. At the distance of M16, $10''$ corresponds to a linear size of 0.1 pc. All observations reported in this paper are labelled using 1950 coordinates, or, where appropriate, using relative offsets.

The submm continuum data were obtained with the JCMT's SCUBA array. This is a submillimetre bolometric camera containing two detector arrays cooled to 0.1 K. These simultaneously view the same patch of sky, about $2.3'$ in diameter, via a beam-splitter. The long-wavelength (LW) array has 37 elements optimised for operation at 850 μm, and the short-wavelength (SW) array has 91 elements for use at 450 μm. The individual bolometer beams are spaced about one beamwidth apart. Three longer wavelength bolometers surround the 850 μm array, offset on the sky from each other by about $2'$, which are used for point-source photometry. The 450 μm array can also be used at 350 μm, and the 850 μm array at 750 μm and 600 μm, with somewhat reduced sensitivity. The data were obtained in the 'Jiggle Map' mode, where the chopping secondary mirror is moved so as to steer each detector beam over a pattern on the sky. This allows fully-sampled maps to be made with points spaced $3.1''$ and $6.2''$ apart for the SW and LW arrays respectively, after on-line re-gridding to an RA / Dec frame. For the observations reported in this paper, the restored half-power beam-widths at 2000, 1300, 850, 750, 450 and 350 μm were $28''$, $18''$, $13''$, $11''$, $7''$ and $7''$ respectively.

Radio observations at 8.69 GHz were obtained using the NRAO Very Large Array (VLA) in the D-configuration, which provided a synthesised beam of $\sim 5''$ HPBW over an area defined by the primary beam of $\sim 5'$. Two short integration ('snapshot') images separated by about 2 hours in time were taken with integration times of ~ 5 minutes across a bandwidth of 100 MHz. The data were edited and calibrated using the AIPS software package and mapped onto a 256 x 256 grid with a pixel size of $2''$. The final images were produced using the routine MX, a version of the CLEAN algorithm, and contained ~ 1000 CLEAN components with a loop gain of 0.1. The maps were then restored with a circular gaussian beam of $8''$ FWHM, giving 4 pixels across the synthesised beam. Further details of the observing set-up are described in Balser et al. (1995).

ISOCAM observations were taken from measurements of the original dataset reported by Pilbratt et al. (1998). Two broad bands were observed; a $4'$ x $4'$ region at a central wavelength of 6.7 μm (LW2), with $1.5''$ pixels and an effective resolution of $2.8''$, and a $4.8'$ x $4.8'$ region at a central wavelength of 14.3 μm (LW3), with $3.0''$ pixels and an effective resolution of $6.0''$. Based on current accumulated ISOCAM experience, the calibration is believed to be accurate to within 10%.

3. Observational results

3.1. SCUBA submillimetre continuum observations

Four field centres were mosaiced together at 850 and 450 μm, and one field centre which covered the three main fingers was observed at 750 and 350 μm. The final images are shown in Fig. 1.

The fluxes obtained with SCUBA at the main peaks, and their photometric errors (in units of Janskys) are listed in Table 2.

The errors quoted in the table are 1σ photometric uncertainties, which are useful for assessing the signal to noise ratio. However, a more conservative estimate of the flux uncertainties based on observations of the planets and secondary calibrators, plus experience of making observations at these wavelengths is typically $2\sigma \sim 5$–7% at 850 μm, 10% at 750 μm, less than 5% at 1350 and 2000 μm, and 25% at 450 and 350 μm.

The 450 μm map, with an effective resolution of $7''$ FWHM, is shown in Fig. 2, overlaid onto the HST image of Hester et al. (1996), and the JCMT CO J = 3–2 (discussed in Sect. 3.2), ISOCAM and VLA (discussed in Sect. 3.5) images of the area which are reported in this paper. The stellar positions measured by Tucholke et al. (1986) and Hillenbrand et al. (1993) were used to solve for the HST and ISO astrometric reference frames.

The Hα and CO overlays in Fig. 2 show that the 450 μm peaks in several of the fingers are displaced back ($\sim 10''$) from the ionised rims of the cloud (Fig. 2a), and that they lie between the molecular hot spots and the photoionised cloud edges (Fig. 2b). However, the ISOCAM overlay (Fig. 2c) shows a more complex situation, where the submm peak in $\mathbf{\Pi}_1$ is co-incident with the brightest 6.7 μm emission, but in $\mathbf{\Pi}_2$ the peak lies about $10''$ further into the finger, away from the bright rim. The VLA overlay (Fig. 2d) is also difficult to interpret: at the head of $\mathbf{\Pi_1}$, the submm peak lies back into the finger relative to the radio free-free emission, whilst in $\mathbf{\Pi}_2$, the submm peak coincides with a bright spot on an apparently limb-brightened finger. The VLA emission is more extended that the ionised gas traced in the Hα image, probably because the radio emission is less affected by the extinction seen in the optical image. Thus the

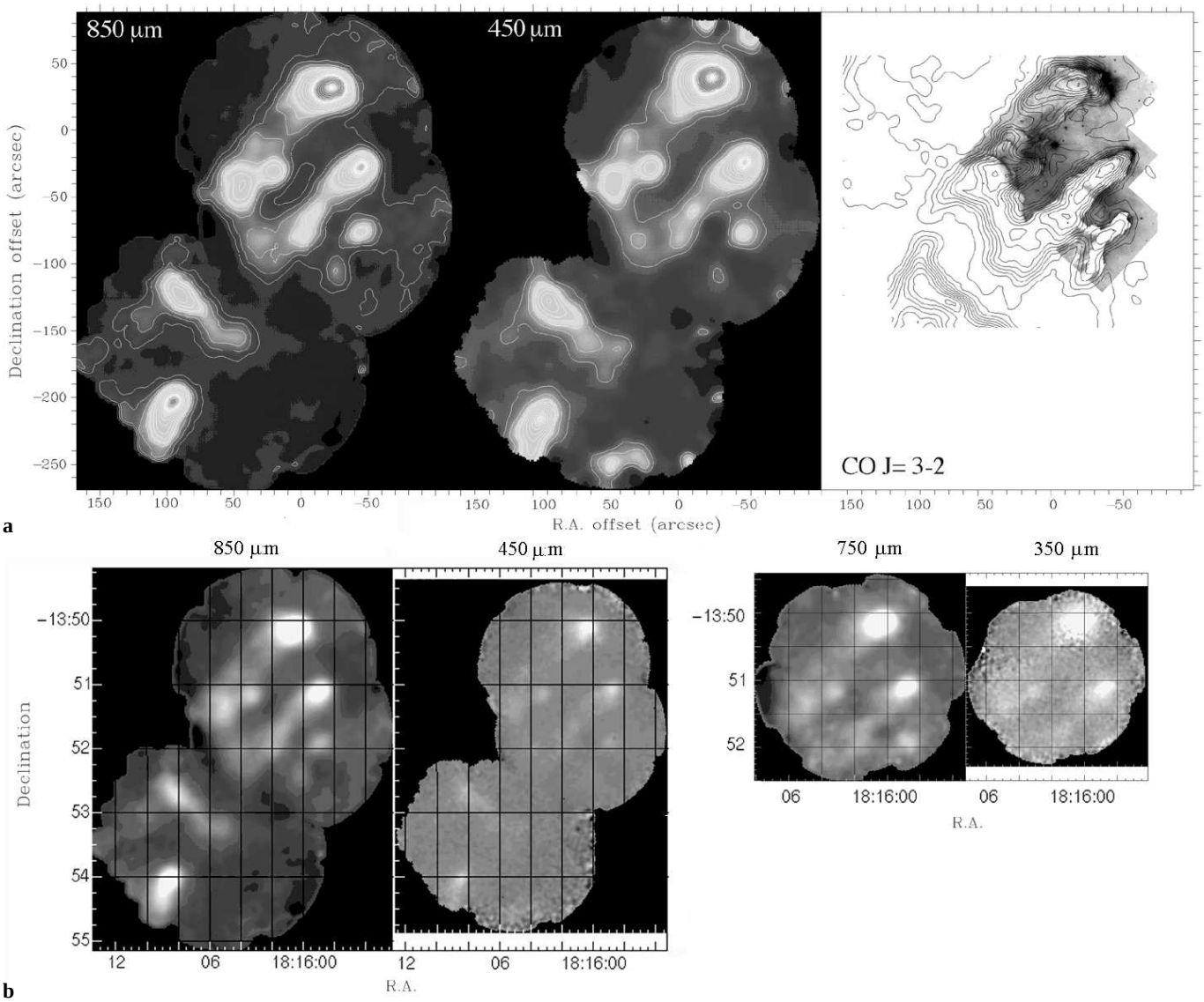

Fig. 1. a Comparison of the SCUBA images at 850 and 450 μm, convolved to an effective resolution of 9″, with the HST Hα image from Hester et al. (1996) and the integrated CO J = 3–2 map (Sect. 3.2 of this paper), **b** greyscale images of the raw images at the four scuba wavebands. This greyscale representation is shown to emphasise the strong cores relative to the weaker material in the fingers

VLA data should trace the front and rear surfaces of the finger providing a complete census of the ionised gas.

In order to measure the mm and submillimetre spectral regions accessible to the JCMT, measurements were made using the photometric pixels of SCUBA, at the positions of the strongest submillimetre continuum peaks. The resultant spectra are shown in Fig. 3, along with greybody spectra fitted using the relationship:

$$S_\nu = \frac{4\pi\kappa_\upsilon}{d^2} \int_0^{R_{ext}} B_\upsilon\left[T_{dust}(r)\right]\ \rho(r)\ r^2\ dr \qquad (1)$$

where T_{dust} is the dust temperature, κ_υ is dust opacity per unit mass column density, B_υ is the Planck function, ρ is the volume mass density – assumed in this case to be constant, R_{ext} is the radius of the emitting region, d is the distance to the Eagle Nebula (André & Montmerle 1994). Photometric measurements were also added from the ISOCAM data, and several points at 60 and 100 μm were estimated from the High Resolution IRAS Galaxy Atlas (IGA–IPAC 1997). These IRAS points should be treated with caution, since the region is confused at the $\sim 1'$ resolution of the image processed IGA maps; hence the IGA data are only useful to set upper limits to constrain the model fits.

To make these fits, the core masses were constrained to those estimated from the $C^{18}O$ observations (see Sect. 3.2), leaving the emissivity, β, and temperature as free parameters. Initial attempts to fit both the absolute values of the fluxes and the spectral energy distribution were made by assuming that the value of β = 1.5. However, this was found to underestimate the flux from the cores in the fingertips at the longest wavelengths

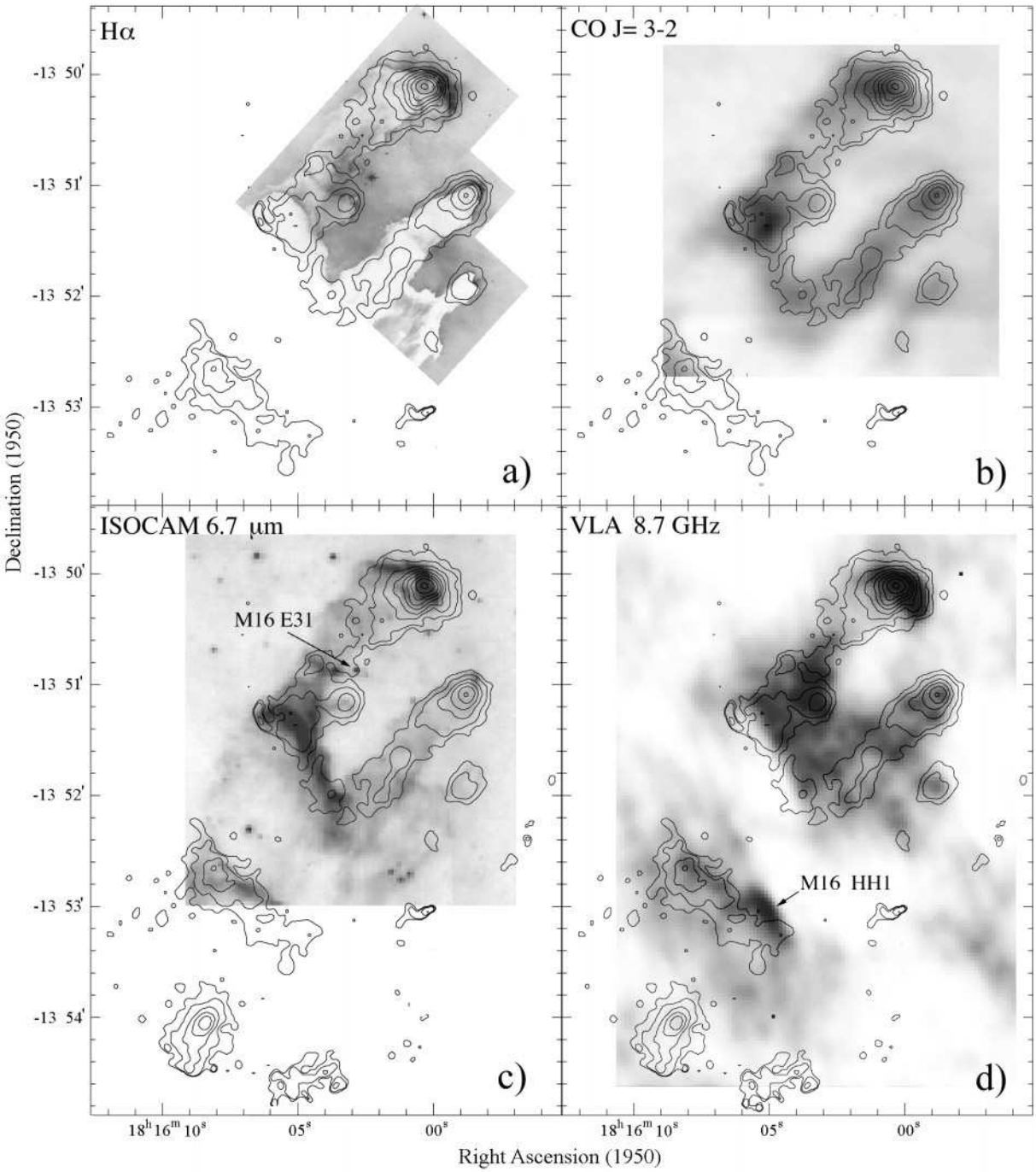

Fig. 2a–d. The SCUBA 450 μm map shown as contours, overlaid onto **a** the HST Hα image of Hester et al. (1996), **b** the CO J= 3–2 integrated emission, **c** the ISOCAM 6.7 μm image, and **d** the 8.7 GHz image. The contour levels on the 450 μm map are 5, 10, 20, 30, 40, 50, 60, 70 and 80 mJy per beam. The lower part of the SCUBA map is omitted from panels **a** and **b**, but included in the *lower panels*. M16 E31 is a bright IR source seen in the ISOCAM images of Pilbratt et al. (1998), and M16 HH1 is an Herbig-Haro object.

by factors of 2–3. It did not appear possible to account for this discrepancy by either calibration errors or beamwidth variations (the data were convolved to the same resolution). We have also considered the possibility that line contamination could influence the estimated dust emissivity. However, as will be seen in Table 3 later, the lines that are detected are all relatively weak, and their integrated emission is insignificant compared to that of the dust continuum. The possibility of multiple dust populations with different grain temperatures remains, although there is no *a priori* reason to assume this in the low temperature material. Finally, it is unlikely that free-free emission is responsible for the long-wavelength excess, as will be discussed in Sect. 3.5. Choosing β = 1.1–1.2 resulted in significantly better fits to the data than values of 1.5–2.0, which are often adopted for mod-

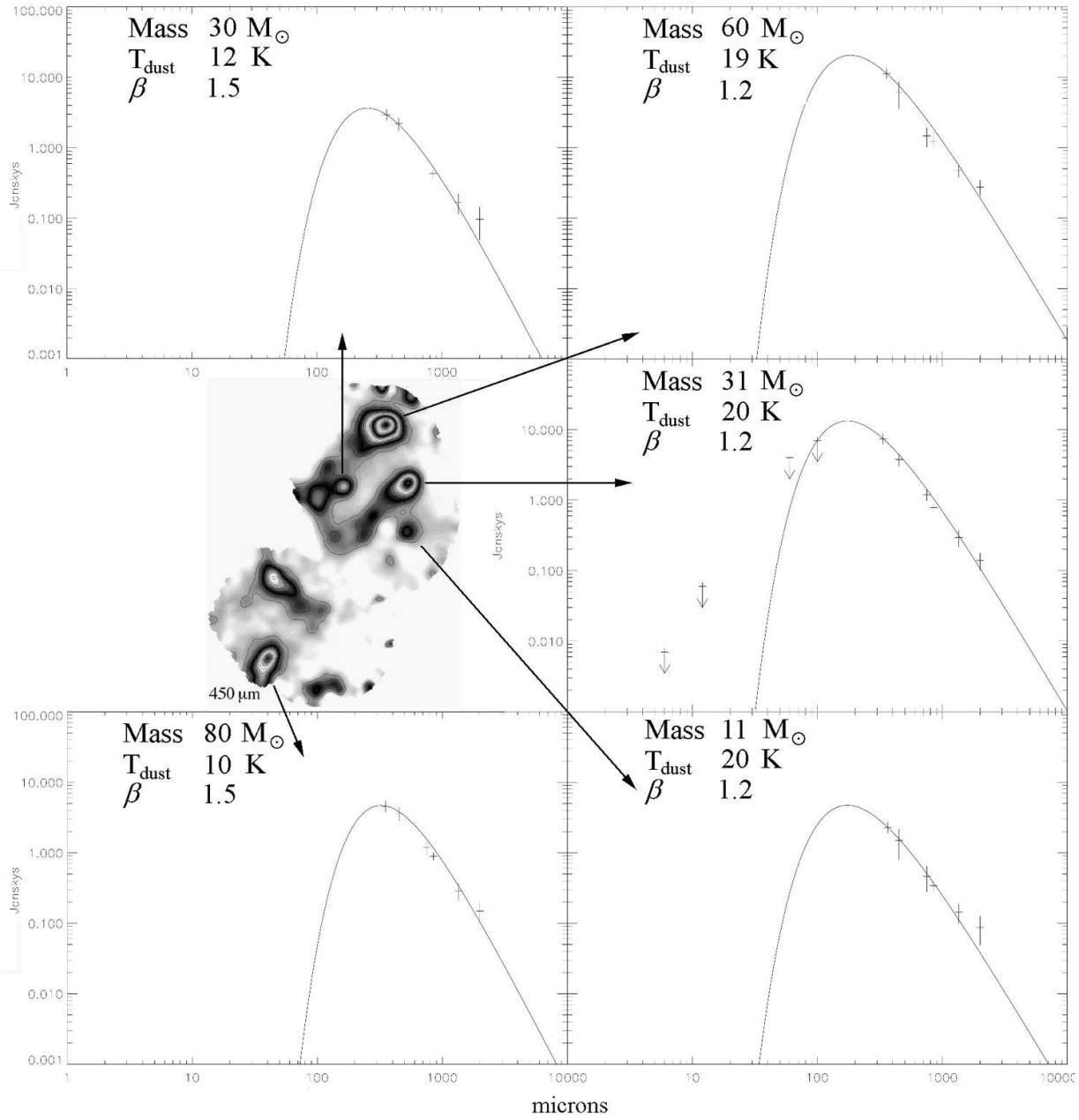

Fig. 3. Submillimetre wavelength spectra of five peaks in the Eagle Nebula from the 450 μm map shown in Fig. 2. The error bars represent the conservative 2σ flux uncertainty. The fitted greybody curves were constrained by adopting the molecular masses (Sect. 3.2), and fitting the temperature and emissivity as free parameters, as described in the text. The IRAS points in the centre right frame are conservative estimates taken from the IRAS IGA survey. Since they involve assumptions about the sizes of the emitting region (which we assume to be the same those estimated from the SCUBA data), and are taken with a large beam ($\sim 1'$ FWHM) in a confused region, they are used only to constrain the fluxes.

elling the properties of clouds (White & Sandell 1995). The most likely conclusion is that to model the submm spectra from the finger tip cores, a relatively low value for the dust emissivity, β needs to be adopted. Such low values of β are possible for coagulated grains or for larger than average grains with thin icy mantles (Mathis & Whiffen 1989, Chandler et al. 1995). Low values of β have also been reported towards a few other protostellar cores (Ward-Thompson et al. 1995, Chandler et al. 1995, and Eiroa et al. 1998), and in circumstellar discs (Beckwith & Sargent 1991). The key result of this modelling is that the submillimetre peaks in the tips of the fingers are constrained to have relatively low dust temperatures $\sim$ 10–20 K. The temperatures of the cores in the fingertips therefore appear to be cooler than both the surrounding warm gas layer ($\gtrapprox$ 60 K) (discussed in Sects. 3 and 4), and the outer shell of hot (250–320 K) material reported from the ISOCAM observations (Pilbratt et al. 1998). These low core temperatures are consistent with our thermal and chemical modelling of a finger, which will be developed in Sect. 4 of this paper. It will be shown that coupled with the higher external temperatures and pressures at the edges of the

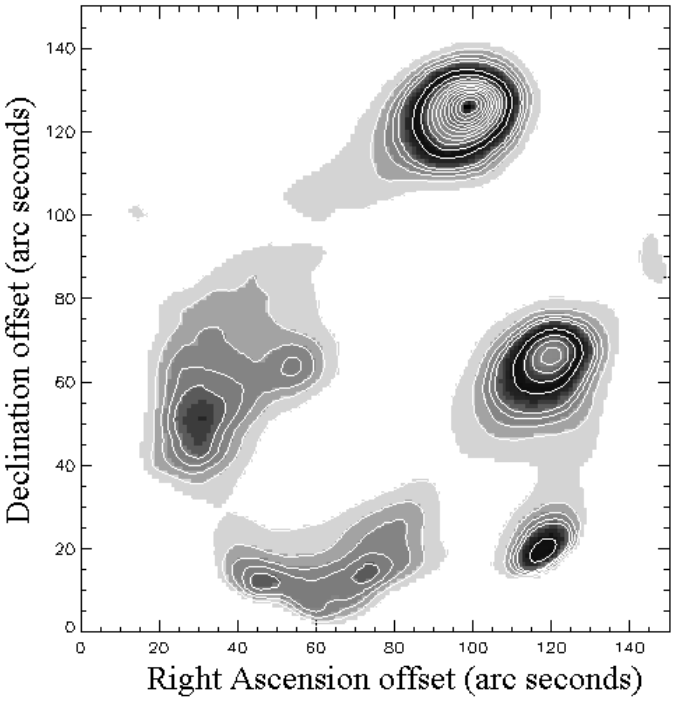

Fig. 4. Richardson-Lucy deconvolution of the 350 μm map. The intensity scale is arbitrary, but linear. The beam profile was estimated by deconvolving maps of the beam which were obtained by scanning the planetary discs of Mars and Uranus, which had diameters of 4.1 and 1.9″ respectively. The adopted beam profile was then used to deconvolve the Eagle Nebula map. The key feature is that these deconvolved images model the sizes of the cores at the tips of the fingers, and show that the two uppermost fingers are marginally elongated along the fingers. Simulations of data with a similar s/n ratio as the real data suggest that the effective resolution of the deconvolved beam for the cores is $\sim 5''$ to first order, although it is in fact dependent on the intensity at a given point in the raw data.

fingers, the consequence will be that the cores in the tips of the fingers will shortly, or have just started to enter a phase of pressure-driven collapse.

The highest resolution SCUBA image at 350 μm was deconvolved from the beam (measured from observations of Mars and Uranus) using the standard Richardson-Lucy technique. The resultant image presented in Fig. 4 shows that several of the cores appear to be elongated along the fingers, with their major axes pointing towards the tops of the fingers. Elongated cores of this kind have previously been reported in the cores of cometary globules (White et al. 1997).

The cores of the submillimetre peak at the tips of $\mathbf{\Pi}_1$ and $\mathbf{\Pi}_2$ can be modelled as 14″ x 20″ FWHM gaussian shaped cores, whose major axes are elongated along the parent fingers. This is equivalent to a linear size of $4.2 \times 6.0\ 10^{17}$ cm.

The submm data can also be used to estimate the column and volume densities of the material in the cores. Concentrating on $\mathbf{\Pi_2}$, because it appears to be a simpler structure than $\mathbf{\Pi_1}$, the gaussian core has a size $\sim 14''$ x 20″ (determined from the maps, and confirmed by the Richardson-Lucy deconvolution). From the modelling above, the submm spectra of the cores are calculated by assuming a mass of 31 $M_\odot$ (this is consistent with the mass derived from the molecular emission, as will be discussed in Sect. 3.2). Assuming that the density is constant in the core leads to a first order estimate for the volume density of $n(H_2) \sim 2.0\ 10^5\ \mathrm{cm}^{-3}$, based on the submm size. This is very close to the value that has been independently reported by Pound (1998).

As a check, the dust mass, and by assuming a dust to gas ratio, the total H_2 mass, can be estimated using the standard relationship:

$$M_g = \frac{F_\nu D^2}{\kappa_m(\upsilon) B_\nu(T_d)} \left(\frac{\tau_\nu}{1 - e^{-\tau}} \right) \left(\frac{M_g}{M_d} \right) \quad (2)$$

where D is the distance to the source, T_d is the dust temperature estimated from the previous fits, $\kappa_m(\upsilon)$ is the dust opacity (mass absorption coefficient per gram of dust), and M_g/M_d is the gas-to-dust mass ratio. Assuming optically thin emission at 850 μm, we adopt $\kappa_m(\upsilon)$ = 1.7 cm^2 g $^{-1}$and β = 1.1 for coagulated dust grains with thin ice mantles for reasons discussed earlier. Assuming a standard dust-to-gas ratio of 150 (Launhardt et al. 1997), and the temperatures estimated from the greybody fits, the lower limits to the mass and particle density in the compact core of $\mathbf{\Pi_2}$ are $\sim 19\ M_\odot$ and $n(H_2) \sim 1.5\ 10^5\ \mathrm{cm}^{-3}$ respectively. The agreement of these estimates points to a relatively cold, compact, massive core, whose parameters based on the submm continuum data agree to within a factor of 2 with values inferred from observations of the molecular emission (see Sect. 3.2).

3.2. CO mapping observations

The peak and integrated intensity maps in the CO *J*= 3–2 line are shown in Fig. 5.

Three narrow fingers of molecular emission extend diagonally across the map, and coincide with the dark regions seen in the HST images of Hester et al. (1996). The CO *J*= 3–2 lines are extremely bright in these fingers, reaching T_{mb} values of ~ 60 K in $\mathbf{\Pi_1}$ and $\mathbf{\Pi_2}$. Although this is a relatively hot CO line source, there is as yet no evidence, e.g. from near-infrared observations, that high-mass star-formation has currently started inside the fingers. There is one bright near-infrared source located $\sim 20''$ E of Walker 367 – the bright star visible on Fig. 5a between $\mathbf{\Pi_1}$ and $\mathbf{\Pi_2}$ – which lies near a minimum in the CO map (also labelled as M16E31 on Fig. 2c).

In each of the three main fingers, the integrated CO emission (Fig. 5b) appears clumpy and fragmented, although the gross structure is resolved by the JCMT beam. Although the integrated map has similarities to the peak temperature map (Fig. 5a), close inspection shows that the integrated CO peaks at the tips of $\mathbf{\Pi_1}$ and $\mathbf{\Pi_2}$ both lie closer to the optical rims than to the positions where the temperature peaks. The lines are all relatively narrow; no compelling evidence was seen anywhere in the mapped region for a discrete molecular outflow source (to the *rms* noise level of $T_{mb} \sim 0.5$ K). Thus despite a plethora of evidence suggesting there are a number of regions which have recently undergone star-formation in the vicinity, there is no

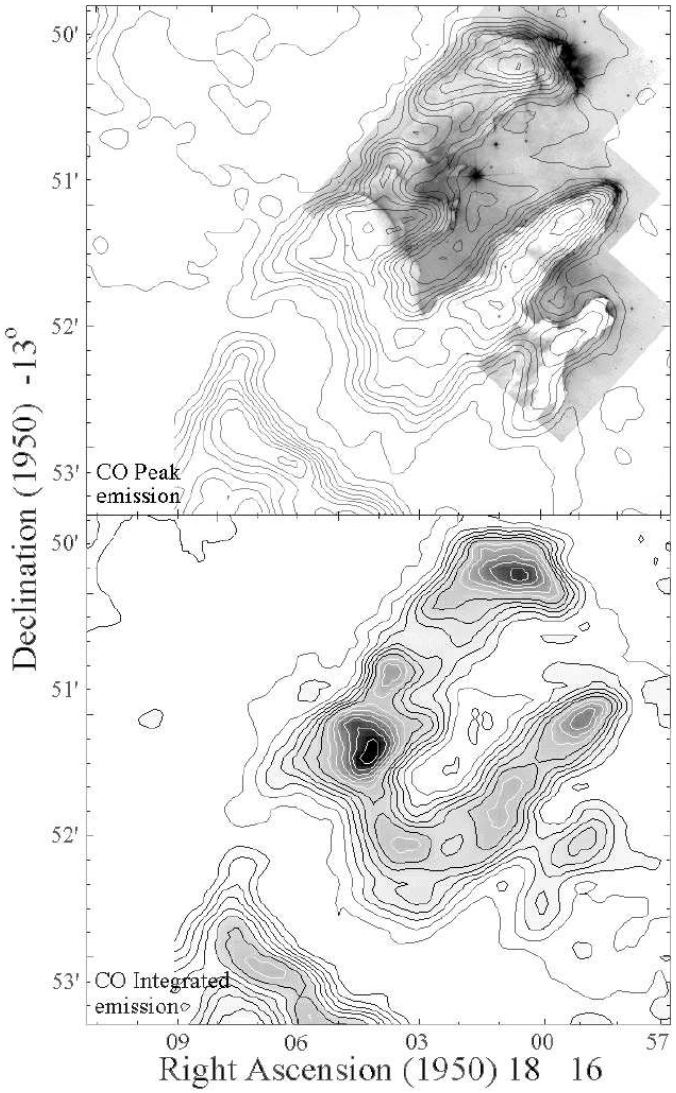

Fig. 5. **a** CO *J*= 3–2 peak intensity map overlaid on the HST composite image of Hester et al. (1996). The lowest contour is at T_{mb} = 6 K, and the contour intervals are at 6 K intervals, **b** CO *J*= 3–2 integrated intensity map integrated from 18–30 km s^{-1}. The lowest contour is at T_{mb} = 17 K km s^{-1}, and the contour intervals are at 23 K km s^{-1} intervals. The ionising stars that illuminate the fingers lie about 2 pc ($\sim 3.5'$) to the NW.

obvious sign of a prominent high-velocity molecular outflow source within the area covered by the CO map.

Spectra of the CO *J*= 3–2 line are shown in Fig. 6.

The linewidths across the CO *J*= 3–2 map are typically in the range 3–5 km s^{-1}, and are mostly single peaked. Towards the base of $\mathbf{\Pi}_1$, the lineshapes are often asymmetrical; probably as a consequence of blending of the emission from $\mathbf{\Pi_2}$ and $\mathbf{\Pi_1}$. The fingers appear to overlap each other on optical images, with $\mathbf{\Pi_2}$ in the foreground (based on the apparently higher optical extinction to the nebular emission than shown by $\mathbf{\Pi_1}$). The velocity structure can be more clearly seen in the CO *J*= 3–2 channel maps integrated over 1 km s^{-1} intervals, which are displayed in Fig. 7.

Viewed in these channel maps, the fingers are made up of a series of clumps which overlap in velocity space. Emission from the gas associated with $\mathbf{\Pi_1}$ extends over the velocity range 23–27 km s^{-1}, whilst $\mathbf{\Pi_2}$ and $\mathbf{\Pi_3}$ are more prominent in the 20–24 km s^{-1} maps. The other molecular material seen towards the western edge of the map from $\sim$28–30 km s^{-1} is not clearly associated with the fingers, and may be physically unrelated gas lying along the line of sight. This range of velocities is similar to that shown in the CO, HI and H II observations reported by Mufson et al. (1981).

Each of the three main fingers was examined for evidence of any systematic velocity gradient, by making position-velocity maps along them, as shown in Fig. 8.

There is evidence for a systematic large-scale velocity gradient of ~ 1.7 km s^{-1}pc^{-1} along the whole length of $\mathbf{\Pi_2}$, although such a trend is not clearly discernible along the other fingers. Similar velocity gradients have been reported from cometary globules, where the morphology is strongly influenced by the external radiation field (Schneps et al. 1980, White et al. 1997).

The optical appearance of $\mathbf{\Pi_1}$ suggests that it is overlapped at its base by $\mathbf{\Pi_2}$. This may lead to the complex velocity structure seen in the CO data, where the peak velocity varies from 21–25 km s^{-1} over a small distance. Consequently, any systematic trends in $\mathbf{\Pi_1}$ over small distances may therefore be masked by the clumpy nature of this particular finger. The velocity shifts of up to $\sim$21 km s^{-1} pc^{-1} claimed by Pound (1998) to trace material flowing along the front and back of the fingers are confirmed by our data. However, because of the difficulty of unambiguously showing that these velocity shifts are due to a *coherent velocity field*, that they trace such large gradients as have been claimed must remain a subject of speculation.

Observations were taken in the C^{18}O *J*= 2–1 and 3–2 lines which should allow column densities to be estimated, and hence the mass of molecular material to be inferred. The C^{18}O *J*= 3–2 map is shown in Fig. 9.

The C^{18}O map is very clumpy and shows several condensed structures, particularly close to the tips of the fingers. This suggests that most of the column density (and mass) resides in small clumps or cores close to the fingertips. The peak C^{18}O *J*= 3–2 main beam brightness temperatures reach $\sim$ 12 K at the tip of $\mathbf{\Pi_1}$, and range from $\sim$ 2–8 K over the rest of the Finger structures. The linewidths are typically $\sim$ 2 km s^{-1} over most of the map, i.e. about half that seen in CO. One striking difference between the CO and C^{18}O distributions is the intense CO peak at offset (+5, +35). This is one of the most intense peaks in the CO map, yet is virtually absent in the C^{18}O map, suggesting that the gas at this point is relativelyhot, but with a low column density.

Spectra in several CO lines and transitions taken at the tip of $\mathbf{\Pi_1}$ are shown in Fig. 10, along with spectra of several other lines:

The intensities (in main beam brightness temperature units – uncorrected for the source brightness distribution) and linewidths of several other lines detected towards the cores at the tips of $\mathbf{\Pi_1}$ and $\mathbf{\Pi_2}$ are listed in Table 3 (with the exception of the CO lines which are complex):

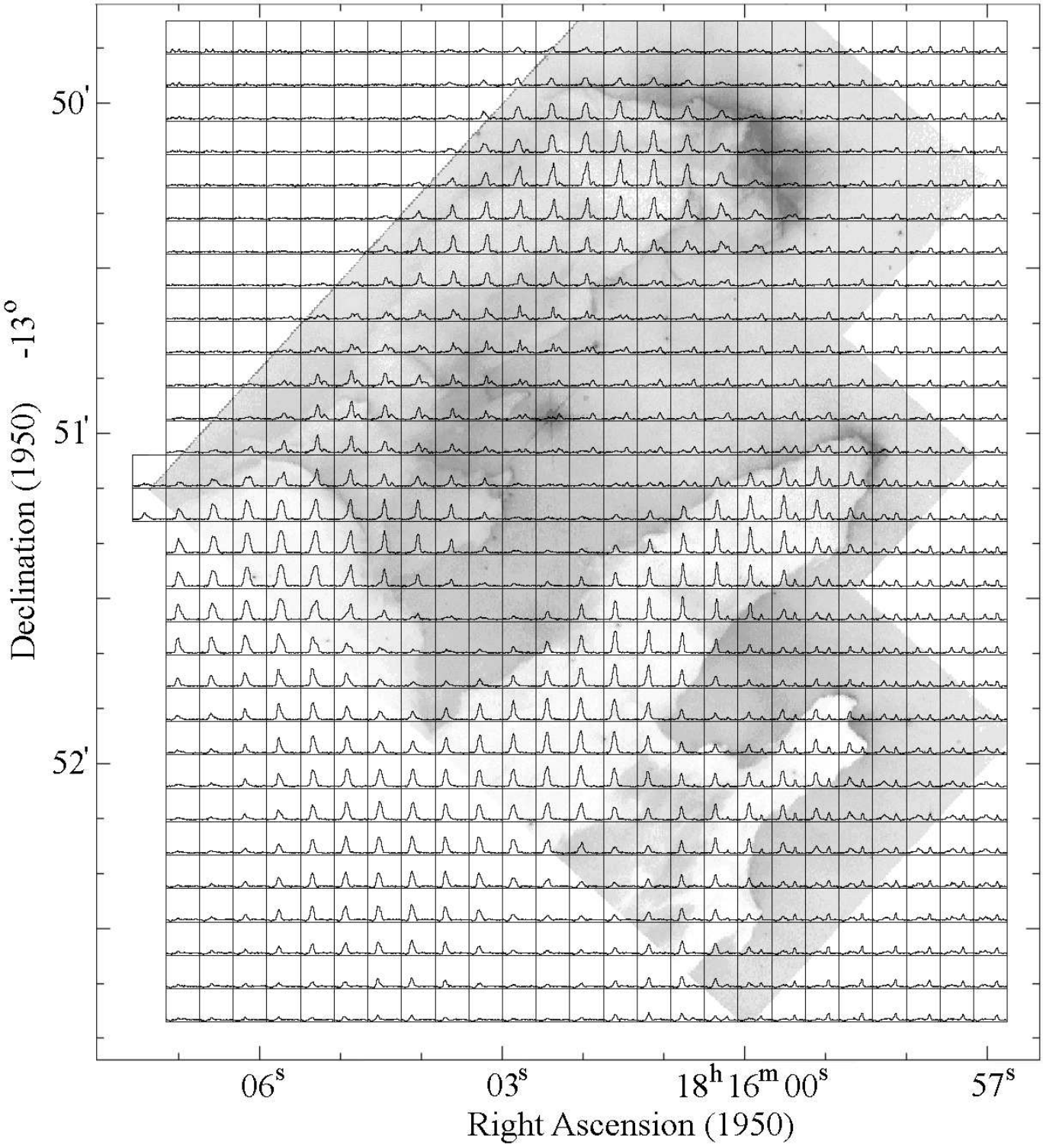

Fig. 6. Overlay of CO *J*= 3–2 spectra on the HST Hα image of Hester et al. (1996). The velocity range of the spectra extends from 20 to 35 km s^{-1}, and the temperature units range in T_{mb} units from -6 to 70 K.

The CO and C^{18}O *J*= 3–2 data were used to estimate the temperatures and column densities, and to infer the masses of the fingers following the techniques discussed in White & Sandell (1995). For this estimate, the abundance [C^{18}O]/[H_2] was assumed to be 1.6 10^{-7}. The total H_2 mass contained within the area covering the C ^{18}O map is $\sim$200 M$_\odot$, of which 95, 56 and 14 M$_\odot$ are contained in $\mathbf{\Pi_1}$, $\mathbf{\Pi_2}$ and $\mathbf{\Pi_3}$ respectively. The remaining mass ($\sim$ 35 M$_\odot$) is associated with the ridge in the southeast corner of the map. Most of the mass of $\mathbf{\Pi_1}$, $\mathbf{\Pi_2}$ and $\mathbf{\Pi_3}$ is located in their tips, which contain $\sim$ 60, 30 and 10 M$_\odot$

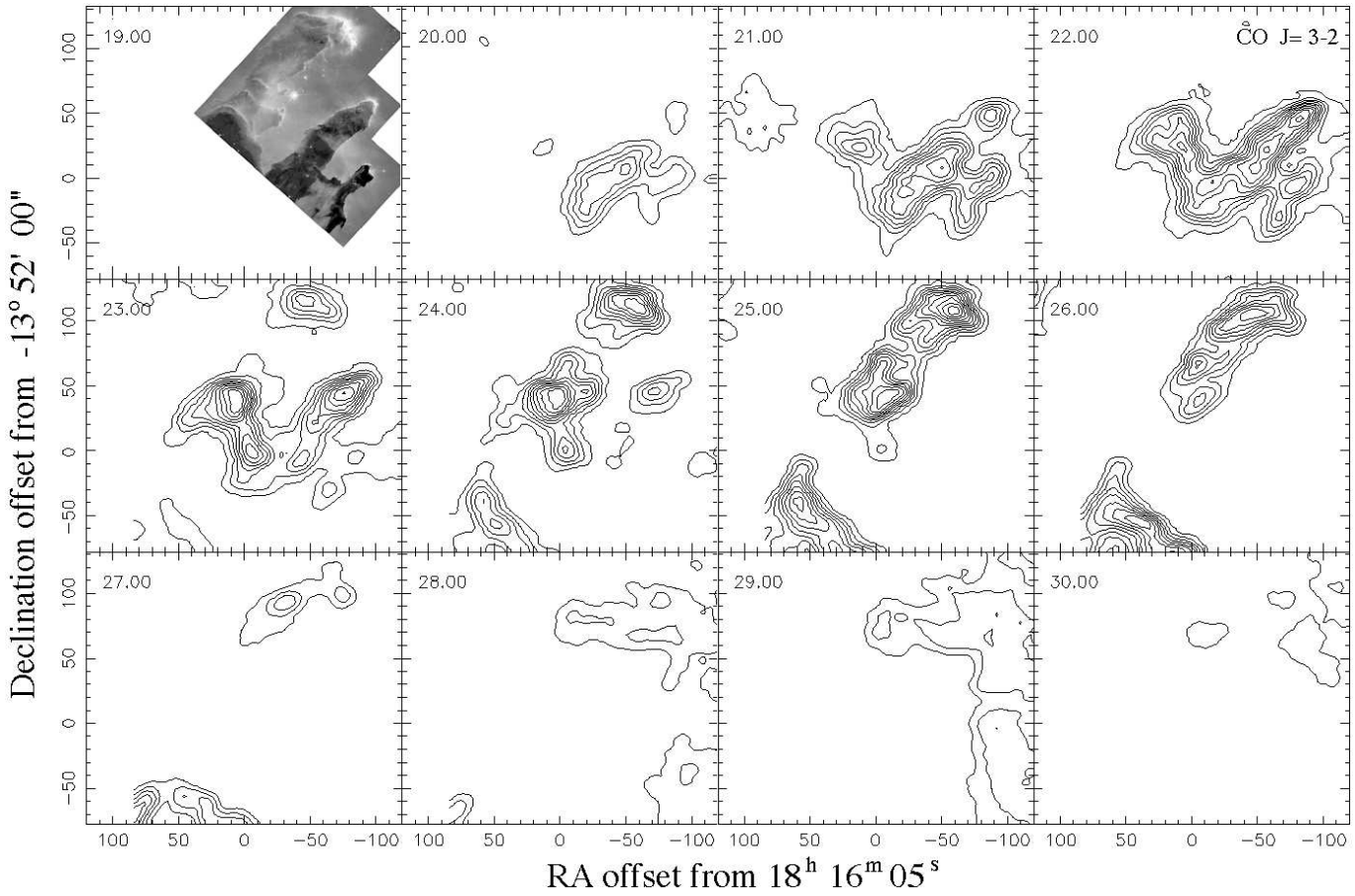

Fig. 7. CO *J*= 3–2 channel maps in 1 km s^{-1} intervals. The lowest contour is at T_{mb} = 6 K km s^{-1}, and the contour intervals are at 6 K km s^{-1} intervals.

Table 3. Gaussian fit line parameters for $\mathbf{\Pi_1}$ and $\mathbf{\Pi_2}$

Line	Transition	$T_{mb}\,dv$ K km s^{-1}	Δv km s^{-1}	v km s^{-1}	$\int T_{mb}\,dv$ K km s^{-1}	T_{mb} K	Δv km s^{-1}	v km s^{-1}	$\int T_{mb}\,dv$ K km s^{-1}
HCN	1–0	2.5	2.5	24.8	6.7	1.8	1.2	22.3	2.4
HCO^+	1–0	2.9	2.2	24.8	6.7	3.1	1.9	22.4	6.3
$H^{13}CO^+$	1–0	0.4	1.0	25.0	0.4	–	–	–	–
CS	2–1	1.3	2.4	24.9	3.5	0.6	1.9	22.4	1.2
$C^{18}O$	1–0	0.5	1.6	24.7	0.9	0.4	2.2	22.3	1.0
^{13}CO	1–0	6.3	2.0	24.9	13.5	5.3	2.2	22.3	12.4
$C^{18}O$	2-1	6.4	1.7	24.8	11.2	3.4	1.4	22.4	5.3
$C^{18}O$	3–2	7.9	1.2	24.9	15.4	6.7	1.7	22.4	12.2
HCO^+	4–3	10.4	2.2	24.9	23.8	6.8	2.1	22.4	14.2

respectively. Thus 63, 54 and 71% of the total masses of $\mathbf{\Pi_1}$, $\mathbf{\Pi_2}$ and $\mathbf{\Pi_3}$ are concentrated into their tips. It is notable that the masses derived from the JCMT data are only about half of those estimated by Pound (1998). To examine this further, spectra and maps were taken in the CO, ^{13}CO and $C^{18}O$ *J*= 1–0, ^{13}CO and $C^{18}O$ *J*= 2-1 and the ^{13}CO and C^{18} O *J*= 3–2 lines using the OSO 20 m, FCRAO 14 m and JCMT telescopes. An analysis of the data from these telescopes give very similar results for the *J*= 1–0 isotopomeric lines: i.e. that they are considerably weaker than might have been predicted, based on their more intense *J*= 2–1 and 3–2 counterparts. Despite attempts to model these ratios using an LVG code, the *J*= 1–0 lines are just consistently low by factors of 2–3. We believe that the *J*= 1–0 line and isotopes may suffer considerably from depletion onto the cold ($\sim$ 20 K) dusty material in the cores. However, the higher excitation lines trace somewhat warmer gas, where the depletion is less effec-

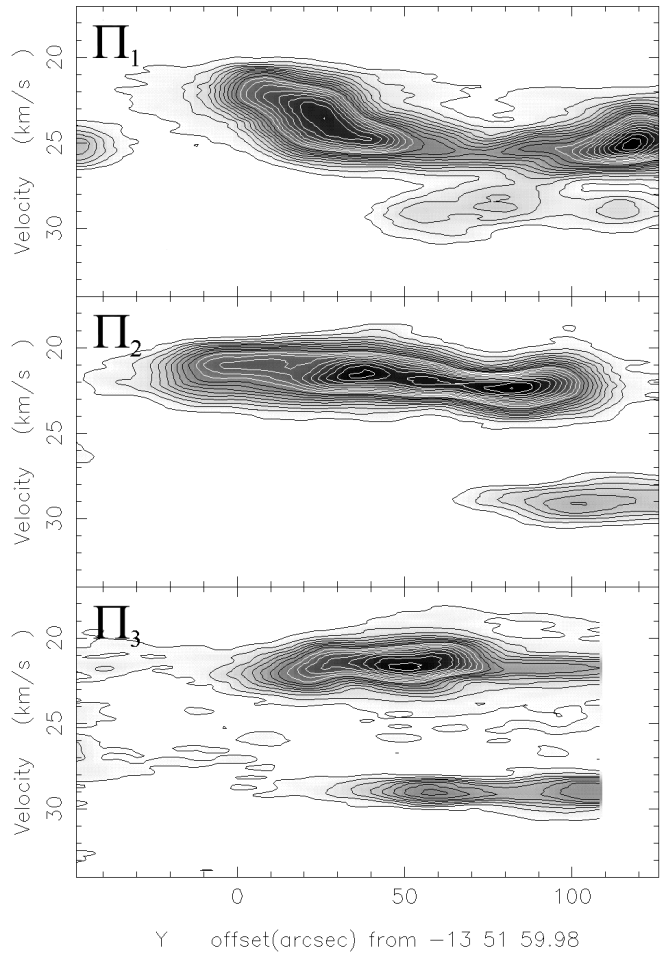

Fig. 8. Position velocity maps in the CO *J*= 3–2 transition along the major axis of the three fingers. These plots were made by rotating the map 42.2 degrees in an anti-clockwise direction, then integrating along the major axis of the fingers, with a 40″ slit centred on the axis of the finger. The tips of the fingers appear on the right hand side of these plots.

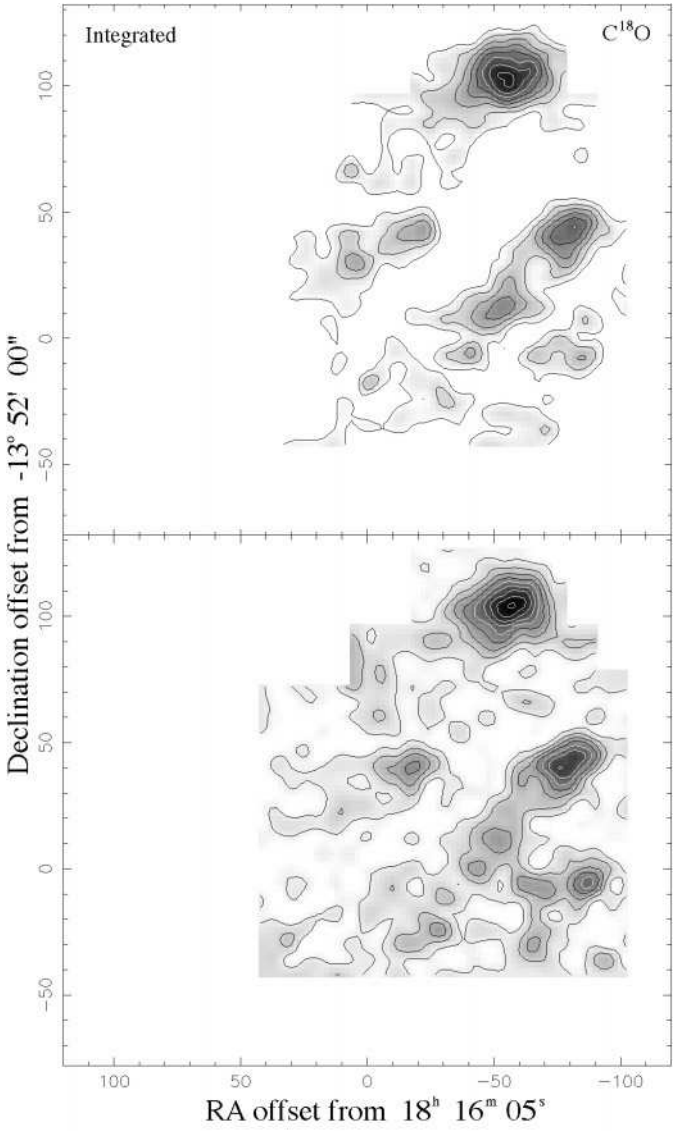

Fig. 9. $C^{18}O$ *J*= 3–2 integrated and peak intensity maps integrated over the velocity interval 20–28 km s^{-1}. The lowest contour level shown on the integrated map is at 2.3 K km s^{-1}, and the contour are spaced at 2.3 K km s^{-1} intervals. On the peak map the first contour has a value of 2.3 K, and the contours are spaced at 1.15 K intervals.

tive. We therefore believe that the estimates of the cloud mass and the opacity using CO *J*= 1–0 line and isotope opacities may be affected by CO fractionation or by depletion onto the cold ($\sim$ 20 K) grains in the core. These observational results and consequences are similar to the conclusions of Hogerheijde (1998), and coupled with isotopic fractionation, have major ramifications for the use of the *J*= 1–0 transitions in estimating cloud masses. We note the problem, and defer further discussion until more quantitative modelling can be performed. We therefore will concentrate on using the *J* = 2–1 and 3–2 ^{13}CO and C^{18}O lines as the more reliable estimator of column densities.

To summarise, the various maps obtained above are all consistent with the masses we have reported above, and appear to be factors of 2–3 times less than those estimated by Pound (1998). Further discussion of the molecular and dust masses of material in the Eagle Nebula fingers will be deferred to a subsequent paper (Deane et al. in prep) which will examine the excitation conditions in more detail than is relevant in this paper.

It is of interest to compare the masses in these tips with their virial masses. An estimate of the ratio of the clump masses to the virial masses is given by the relationship:

$$\frac{M_{clump}}{M_{virial}} = \frac{G \sum\limits_{clump} T_{mb}\ dv}{5\ r\ \sqrt{\frac{\Delta v^2}{8\ \ln 2}}} \qquad (3)$$

This ratio has values of 0.55, 0.97 and 0.6 respectively in the three tips of the fingers, so that each of the tip clumps appear to be close to gravitational stability, given the inherent uncertainties in this simple estimate. A more realistic estimate of the stability of the clumps, which considers surface pressure and the support of internal magnetic fields will be given in Sect. 6. It should be noted at this stage that there is no compelling evidence for the

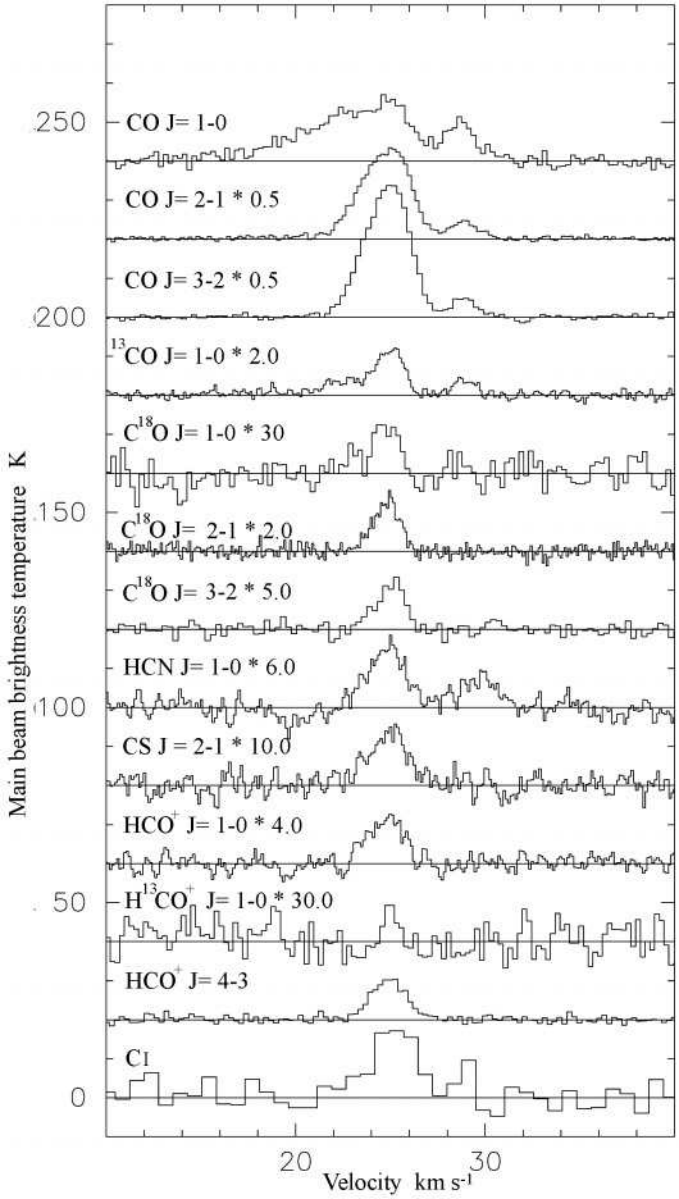

Fig. 10. Spectra towards the core at the tip of $\mathbf{\Pi_1}$. For presentation purposes, the intensities of various lines have been scaled as indicated on the figure: thus CS *J*= 2–1 * 10 means that the line intensity is shown at 10 times its true value. The velocity component at 29 km s^{-1} may be unrelated line of sight material. It is clearly seen that the *J*= 1–0 CO and isotopomeric transitions appear weak relative to the other CO lines (note the factor of two difference in the scaling between the *J*= 1–0 lines and the other transitions).

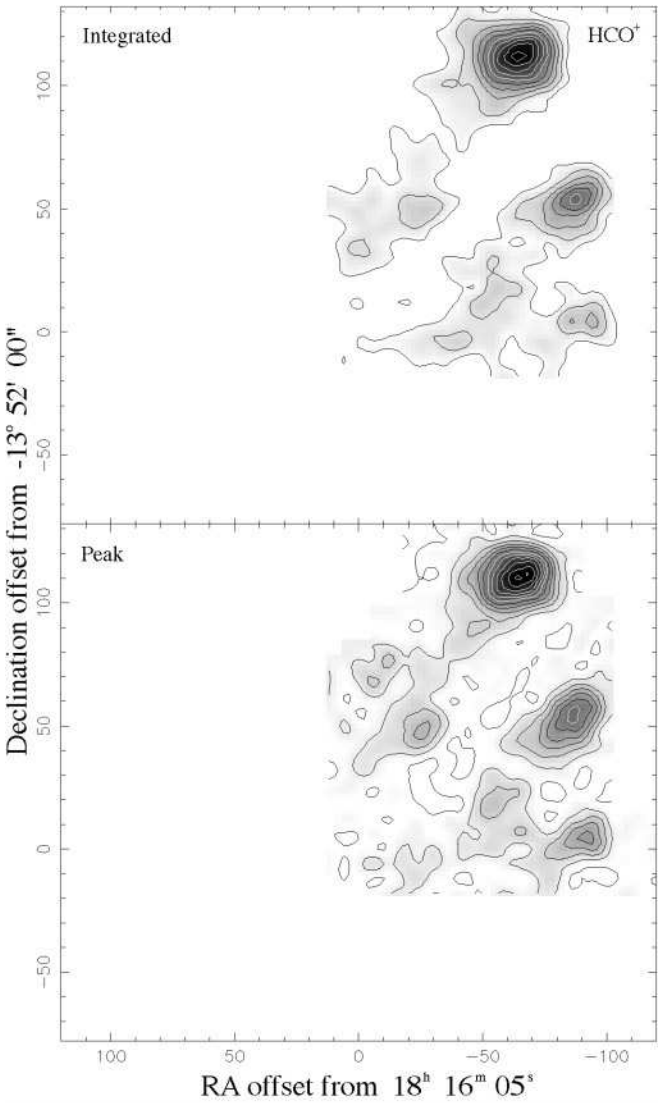

Fig. 11. HCO^+ *J*= 4–3 integrated and peak and intensity maps over the range 20–28 km s^{-1}. The lowest contour on the the integrated map is at 2 K km s^{-1}, and the contour intervals are at 2 K km s^{-1} intervals, and on the peak map is T_{mb} = 1.0 K, and the contour intervals are at 0.75 K intervals.

rapid gravitational collapse of the cores in the tips of the fingers. As will also be discussed later (Sect. 4.3), it is likely that the CO line emission comes predominantly from a hot sheath of gas close to the surfaces of the fingers. In this scenario the $C^{18}O$ lines trace cooler material inside the fingers: the consequences of this will be an increase of the gravitational potential energy of the cores.

Assuming that the clumps at the fingertips are symmetric, their volume densities, $n(H_2)$, are $\sim 2.3\ 10^5$ and $2.0\ 10^5$cm $^{-3}$ respectively for $\mathbf{\Pi_1}$ and $\mathbf{\Pi_2}$, compared with nearby material in the fingers where $n(H_2) \sim$ 3–5 10^4cm^{-3}. It therefore appears that the clumps at the tips are already relatively centrally condensed, and should have free-fall times $\gtrapprox 10^5$ years.

3.3. HCO^+ observations

As discussed earlier, the HST pictures show that material at the edges of the fingers is strongly photo-ionised. Consequently observations were made in the molecular ion HCO^+ in the *J*= 4–3 line, shown in Fig. 11, to compare with the other molecular data.

The HCO^+ map has a very similar shape to that of the $C^{18}O$ map, suggesting that the two species are well mixed, and trace the material in the same regions. This contrasts with observa-

Table 4. Column densities and abundances at the finger tips

Offset	$N_{col}(HCO^+)$	$N_{col}(C^{18}O)$	$N_{col}(CI)$	$X(HCO^+)$	[CI]/[CO]
$''$	cm^{-2}	cm^{-2}	cm^{-2}		
−60,108	$1.2\ 10^{13}$	$9.2\ 10^{15}$	$7.5\ 10^{16}$	$2.1\ 10^{-10}$	0.02
−84,42	$6.0\ 10^{12}$	$6.4\ 10^{15}$	$5.4\ 10^{16}$	$1.5\ 10^{-10}$	0.02
−84,0	$3.2\ 10^{12}$	$1.3\ 10^{15}$	$4.5\ 10^{16}$	$3.9\ 10^{-10}$	0.07
−24,36	$6.1\ 10^{12}$	$1.6\ 10^{15}$	$3.4\ 10^{16}$	$6.1\ 10^{-10}$	0.04

tions of HCO^+ towards other sources by Gibb & Little (1998) and Hogerheijde (1998), who suggest that HCO^+ may be a better tracer of a protostellar envelope than $C^{18}O$ – clearly conditions in the two sources are rather different – in the Eagle Nebula, both $C^{18}O$ and HCO^+ track each other fairly closely, and there does not appear to be strong evidence for a relative spatial abundance variation, such as that which might be a result of strong C ^{18}O depletion onto grains. The HCO^+ line intensities are also relatively high, approaching $T_{mb} \sim 10$ K at the tip of $\mathbf{\Pi_1}$, and 7 K and 4 K at the tips of $\mathbf{\Pi_2}$ and $\mathbf{\Pi_3}$. The column density of HCO^+ was calculated from the relationship for the *J*= 4–3 transition:

$$N_{tot}\left(HCO^+\right) = \frac{5.65\ 10^{10}\left(1+\frac{0.72}{T_{ex}}\right)\int T_{mb}\ dv}{\left(1-\exp\left(-\frac{12.8}{T_{ex}}\right)\right)\quad \exp\left(-\frac{12.8}{T_{ex}}\right)} \times\frac{\tau}{1-\exp(-\tau)}\quad cm^{-2} \qquad (4)$$

These column densities were then used with the CO and $C^{18}O$ data to estimate the various abundances (where the H_2 column density is estimated from the $C^{18}O$ data as described earlier) – the results are summarised, along with those estimated for CI in the next section, in Table 4:

3.4. CI observations

A map made in the CI $^3P_1$– $^3P_0$ line is shown in Fig. 12.

The line temperatures, linewidths and integrated emission were measured at each point within the CO, $C^{18}O$ and CI data cubes, after convolving the CO and CI data to have the same spatial resolution as the $C^{18}O$ data. These data were then used to estimate the CI and CO column densities over the mapped region using standard methods for estimating column densities summarised in White & Padman (1991), White & Sandell (1995) and White et al. (1995). The variation of the CI and CO column abundances has been used in the past to probe the photodissociated outer edges of molecular clouds. The CI abundance relative to CO, [C I] / [CO], is shown in Fig. 13.

There is a clear tendency for the [CI]/[CO] values to increase in regions where the column density is less – with the ratio increasing from ~ 0.02 in the highest column density material, to ~ 0.1 in the lowest. This is similar to the trend noted towards other molecular clouds (Keene 1987, White & Sandell 1995, White et al. 1995, Minchin et al. 1995) which has been interpreted as evidence for an increasing [C I/CO] abundance ratio at their UV exposed edges.

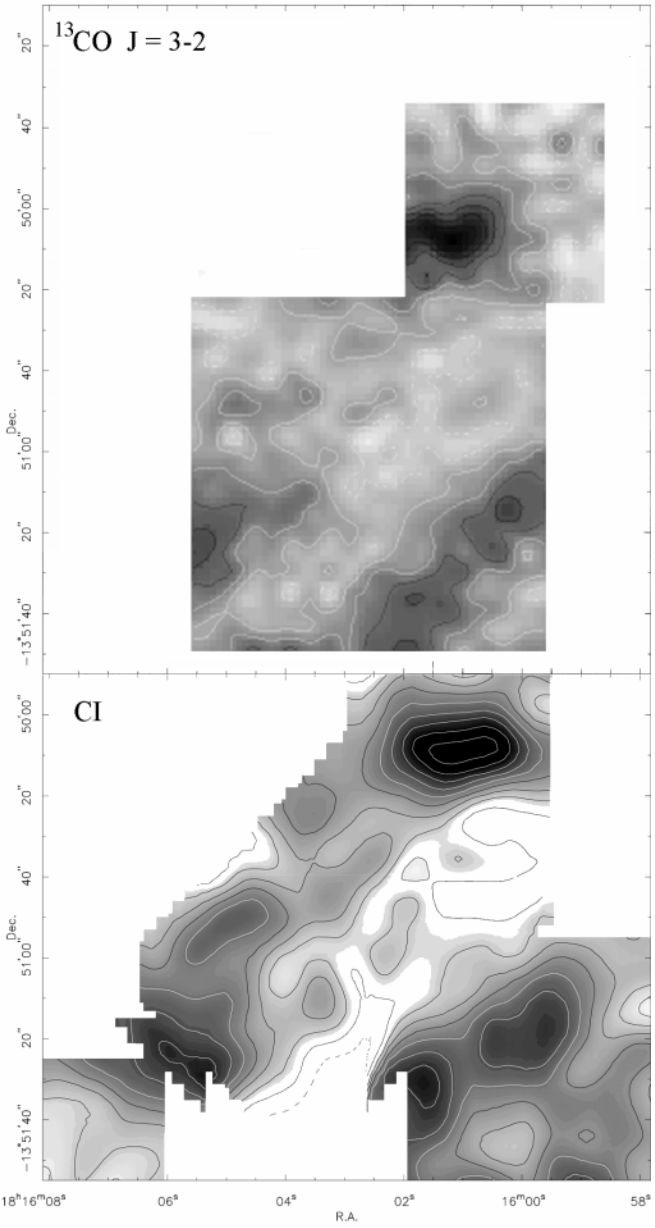

Fig. 12. *Top* ^{13}CO J=3 – 2 integrated emission over the range 20–28 km s^{-1}. The lowest contour on the map is T_{mb} = 10 K km s^{-1}, and the contour intervals are at 10 K km s^{-1} intervals. C I $^3P_1$ - $^3P_0$ integrated intensity map over the range 20–28 km s^{-1}. The lowest contour on the map is T_{mb} = 3.3 K km s^{-1}, and the contour intervals are at 3.3 K km s^{-1} intervals. Note that the tip of $\mathbf{\Pi_3}$ lies just off the *bottom* right hand edge of this map.

3.5. Radio continuum observations

During the analysis of the submillimetre continuum data, the relatively high fluxes at the longer wavelengths (compared to a single temperature greybody fit) led to speculation as to whether the longer mm wavelength excess (over blackbody emission) was due to free-free emission. To check this, data obtained with the VLA (Balser et al. 1995) were examined, to extend the spectral coverage into the radio spectrum. Although there is no information on the radio spectral index of the emission, it is

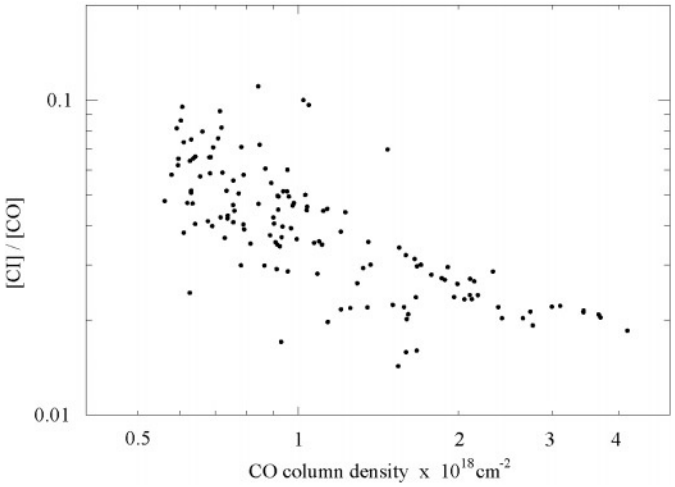

Fig. 13. Plot showing the [CI]/[CO] abundance variations in the mapped area. Note that both axes are logarithmic.

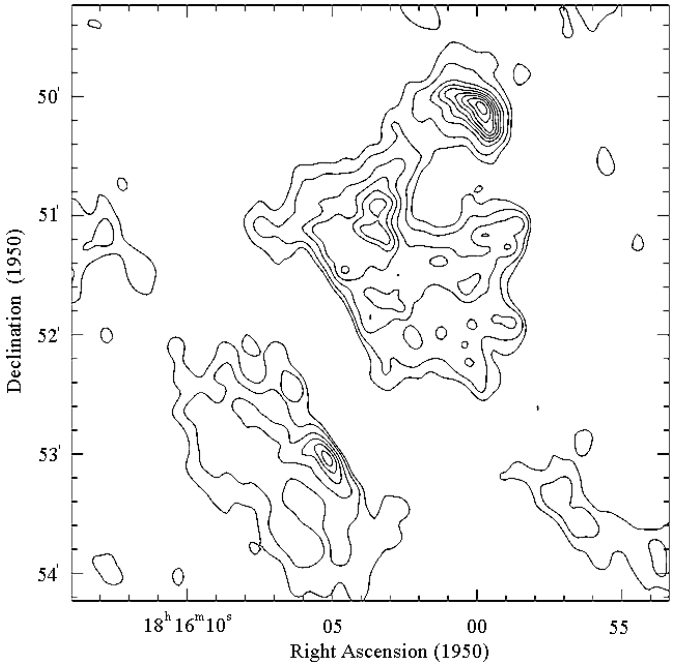

Fig. 14. Contour map of the free-free emission measured at 8.69 GHz with the VLA in the D array configuration (see Fig. 2d) for a greyscale representation). The contours are at 1, 2, 4, 6 . . . 18 mJy / beam.

highly likely that it traces the optically thin free-free emission from ionised gas at the surfaces of the fingers. The VLA map is shown as a contour map in Fig. 14 (see Fig. 2 for a grey-scale representation).

The VLA map shows $\mathbf{\Pi_1}$ and $\mathbf{\Pi_2}$ very clearly, as well as an indication of emission from $\mathbf{\Pi_3}$. The most intense radio emission comes from the tip of $\mathbf{\Pi_1}$, where the distribution resembles the structure seen in the ISOCAM and optical data. The radio emission from $\mathbf{\Pi_2}$ shows evidence for limb-brightening along both sides of the finger (seen as the two peaks close to the tip of $\mathbf{\Pi_2}$ in Fig. 14, but more clearly seen on the greyscale representation in Fig. 2d)), but any such limb-brightening is less prominent towards $\mathbf{\Pi_3}$. In addition to emission from the fingers, radio emission can also be seen from the ridge several arc minutes SE of the fingers. This is visible in both the CO and SCUBA data, and contains the Herbig-Haro object HH 216. Integrating the free-free emission from the fingers we estimate the integrated and peak fluxes from $\mathbf{\Pi_1}$, $\mathbf{\Pi_2}$ and $\mathbf{\Pi_3}$ as 123, 48 and 6 mJy, and 17, 7 and 5 mJy/beam respectively.

It is widely accepted that the UV radiation and winds from OB stars can affect the structure, dynamics and evolution of the edges of molecular clouds on which they impinge. The dominant processes include interaction with the expanding Strömgren spheres around the stars, photoevaporation, or disruption by shocks resulting from an overpressure of the hot ionised outer parts of clouds, on their lower pressure interiors – leading to a shock wave driving in towards the core. The structure of these regions is affected by the clumpy distribution of molecular cloud material, which can allow UV photons to penetrate deeply into the edges of clouds.

As UV radiation falls onto the outer layers of clouds, the low-density gas at the surfaces is photo-evaporated. The ionised material will flow outwards where the density gradient is largest. This often leads to the appearance of 'rays' or striations emanating from the cloud surface. As this lower density material becomes photo-evaporated, dense clumps of gas deeper inside the cloud become exposed. Examples of this can be seen along the edges of the Eagle's fingers, many of which have EGG's close to their tips. Thus these are primordial clumps inside the cloud, whose presence is revealed as surrounding low-density material is removed. The surfaces of these primordial clumps themselves become photo-ionised, and may themselves be the sites of future star-formation.

As shown by Oort & Spitzer (1955), and subsequently developed by Bertoldi & McKee (1990), Lefloch & Lazareff (1994) and Megeath & Wilson (1997), an equilibrium is rapidly set up in which photo-ionised material streams off the surface of an UV irradiated clump. Some fraction of the hydrogen atoms recombine, self-shielding the neutral gas from the ionising radiation. A small fraction of the ionising photons do however manage to penetrate through to the neutral gas and to ionise material at the base of the flow. Megeath & Wilson (1997) show that the ratio of the total ionising flux to that which penetrates to a depth where it can ionise the neutral gas, *q*, is given by the relationship:

$$q = \left(0.1 \frac{S\ r\ \alpha}{4\pi\ R^2\ \ c_{II}^2}\right)^{0.5} \quad (5)$$

where *S* is the Lyman photon production rate of the illuminating stars, which are located at a distance *R* away from a spherical clump of radius *r*, where α is the recombination coefficient and c_{II} is the sound speed in the ionised gas. Using values appropriate to the Eagle Nebula, $q \sim 50$. Thus, assuming that the radio emission is produced within the photo-evaporating flow, the measured recombination rate should provide a good check on the rate of ionising photons incident on the surfaces of the fingers.

Following the work of Bertoldi (1989), Lefloch & Lazareff (1994) and Lefloch et al. (1997), the flux, S_ν, at 8.69 GHz is related to the total ionising flux Φ (cm^{-2} s^{-1}) by the relationship:

$$\left(\frac{S_\nu}{mJy}\right) = 2.59\ 10^{-10}\ \Phi\ \left(\frac{T_e}{10^4\ K}\right)^{-0.35}\ \Omega \qquad (6)$$

where T_e is the electron temperature (which is adopted to be 6000 K (Balser et al. 1995)), and Ω is the solid angle of the emitting region. Similarly, the electron density n_e cm^{-2}, will be given by:

$$n_e = 4\ 10^7\ \left(\frac{S}{\Omega\ t}\right)^{0.5} \qquad (7)$$

where t is the thickness of the shell of ionised gas and electrons which surrounds the photo-ionised cloud (we adopt $t \sim 6\ 10^{16}$ cm, based on the discussion by Lefloch et al. (1997)).

Using these relationships we estimate $\Phi \sim 5\ 10^{10}$, $2\ 10^{10}$ and $9\ 10^9$ cm^{-2} s^{-1} for $\mathbf{\Pi_1}$, $\mathbf{\Pi_2}$ and $\mathbf{\Pi_3}$ respectively, and electron densities of $\sim$500, 320 and 100 cm^{-3} respectively. The ionising flux estimated from the radio observations can be compared to the photon flux expected from the ionising stars. Hester et al. (1996) suggest that the ionising flux is dominated by a single O3.5 star and three O5.5 stars located 2 pc away, which together provide a total photon flux $\sim 2\ 10^{50}$ s^{-1}. This would correspond to an ionising flux at the surface of the pillars of $\sim 1.5\ 10^{11}$ photons s^{-1} cm^{-2}. The photon rate with energies from 6 and 13.6 *eV* (the spectral range where most of the ionisation occurs) is then estimated from stellar atmosphere models. Using a Kurucz model (Kurucz 1979), the fraction of UV photons with energies in the appropriate range (6–13.6 *eV*) is $\sim$35% of the total photon flux, which then leads to a value of $G \sim 1700$ G_0 **[**G_0 is the 'standard FUV interstellar radiation field' taken from Habing (1968)**]**. Thus the effective ionising flux at the surface of the fingers is $\sim 1.75\ 10^{10}$ photons s^{-1} cm^{-2}, which is close to that inferred above from the VLA data. Also, it is easy to show from the VLA data that the electron densities exceed the critical density of $\sim$25 cm^{-3}, above which an ionised shell should develop around a neutral cloud (see Lefloch & Lazareff 1994).

4. Chemical and thermal modelling

In order to understand its physical, thermal, chemical and dynamical structure, a simplified chemical and thermal model of one of the fingers was developed. This is used to understand factors which will help predict its future evolution and potential for forming star(s). $\mathbf{\Pi_2}$ was chosen as a basis for this modelling, since it seems to have a simpler structure than $\mathbf{\Pi_1}$, whose appearance seems to be affected by overlapping finger material. The geometrical form of the cloud model is shown in Fig. 15. The cloud model consists of a cylindrical column of gas with a spherical core embedded towards its tip. The spherical core has an internal density profile with a maximum number density of $n(H_2) \sim 2\ 10^5$ cm^{-3}, decreasing to $n(H_2) \sim 2\ 10^4$ cm^{-3}, which is the average value of material in the finger. These estimates allow a simple first order model of the dense clumps observed near the fingertips to be computed.

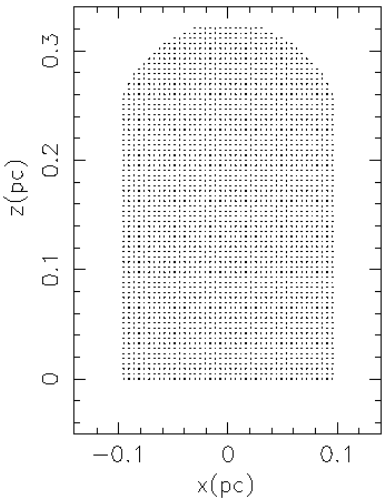

Fig. 15. Geometric configuration adopted for the model finger, showing the size and shape used, along with the co-ordinates of the sample points used for the calculation grid.

It was assumed that this column of gas is subjected to anisotropic heating by the FUV field, with an incident ionising flux corresponding to $\sim 2\ 10^3$ G_0 on the top of the finger, and ~ 10 G_0 on the sides. The finger receives no illumination from below, since it appears to be well shielded from that direction. Starting from the density and UV field, the chemical and thermal structure of the cloud can be estimated, using the thermal and chemical models described below.

4.1. Thermal modelling

The thermal model used in the calculations presented here is similar to that used in Nelson & Langer (1997), but with some extensions described in 4.1.1 and the Appendix. We describe each contributor to the thermodynamic balance of the gas in turn, starting with those processes responsible for heating the gas, followed by the cooling mechanisms. We note that these models are designed to examine the cloud properties interior to the ionisation front, so we do not attempt to model the outer region of the cloud.

4.1.1. Grain photoelectric heating

Ignoring gas heating by the EUV field at the ionisation front, the dominant contribution to the heating of the gas in the outer layers of the M16 nebula is then through the photo-ejection of electrons from dust grains. This is caused by the incident FUV flux from the group of O stars located about 2 pc above the three gaseous columns. We adopt the approach used in Nelson & Langer (1997) for modelling this process, with the modification that the effect of grain charging on the grain's work function is now included, since significantly higher UV fields are being considered in this work.

The photoelectric heating rate is given by (Hollenbach et al. 1991):

$$\Gamma_{ph} = 4.86\ 10^{-26}\ n_0\ G_0\ \exp(-k_{uv}A_v)\ \ f_{grain} \tag{8}$$

where n_0 = n (HI) + 2 n (H_2), the total number density of hydrogen atoms, G_0 is the standard interstellar UV field (Habing 1968), A_v is the visual extinction, κ_{uv} is a factor which accounts for the increased extinction of the UV field due to dust grain scattering, and f_{grain} accounts for the reduced efficiency of heating when the grains become positively charged, leading to an increase in the grain work function. The above formula is usually applied to 1-D slab models of clouds, but in this work we are interested in developing a cloud model in which the 3-D nature of the object is approximated. We therefore adopt the approach used in Nelson & Langer (1997), and calculate the heating at an arbitrary point in the cloud as if it were coming from six directions, namely along the positive and negative Cartesian co-ordinate directions. When computing the photoelectric heating rate at a point in the cloud, we integrate along each of these Cartesian co-ordinate directions to the cloud surface in order to calculate six values of A_v. An approximation to the previous equation is then used to calculate the heating:

$$\begin{aligned}\Gamma_{ph} \ = \ & 4.86\ 10^{-26} n_o f_{grain} \frac{1}{6} \Big[G_o(x^+) e^{-\tau_{uv}(x^+)} \\ & + G_o(x^-) e^{-\tau_{uv}(x^-)} + G_o(y^+) e^{-\tau_{uv}(y^+)} \\ & + G_o(y^-) e^{-\tau_{uv}(y^-)} + G_o(z^+) e^{-\tau_{uv}(z^+)} \\ & + G_o(z^-) e^{-\tau_{uv}(z^-)} \Big]\end{aligned} \tag{9}$$

The heating at any point within the cloud is then estimated by considering the six heating rates coming from the positive and negative *x*, *y*, and *z* directions. Note that the value of G_0 clearly will change with direction, so that anisotropic UV fields may be modelled using this formula. When running the models, we assume that the cloud is primarily illuminated from above (the positive *z* direction), to a lesser degree from the sides of the cloud (*x* and *y* directions), and receives no illumination from below (negative *z* direction). The values of G_0 have typical values of G_0 (z +) = 2000, G_0(x +/-) = G_0(y +/-) = 10, G_0(z -) = 0, where the +/- superscripts refer to the positive and negative co-ordinate directions.

4.1.2. Gas-dust thermal exchange

When the kinetic temperature of the gas molecules differs from that of the dust grains, there is a thermal energy exchange through collisions. We assume that when a molecule hits a dust grain, it sticks to it, and is later re-emitted carrying away energy $\sim 3/2\ T_d$, where T_d is the dust temperature. The rate of energy exchange between the gas and dust can then be simply estimated following Goldsmith & Langer (1978), where the energy exchange rate is given by:

$$\Lambda_{gd} = 2.4\ 10^{-33}\ T_g^{\frac{1}{2}}\ \ (T_g - T_d)\ \ n_o^2\ \mathrm{ergs\,cm^{-3}\,s^{-1}} \tag{10}$$

It should be noted that gas-dust interactions only play a major role in the thermal evolution of the gas where the number density $n_0 \sim 10^5\ \mathrm{cm^{-3}}$, as a consequence of the quadratic dependence on n_0.

We employ the expression suggested by Hollenbach et al. (1991) to calculate the dust temperature:

$$\begin{aligned}T_d \ = \ & (8.9\ 10^{-11}\ \upsilon_0\ G_0\ \exp(-\kappa_{uv}A_{uv}) + \ 2.7^{\ 5} \\ & + 4.4\ 10^{-2}\ \ \left[0.42 - \ln(3.5\ 10^{-2}\ \tau_{100}\ T_0)\right] \\ & \times \tau_{100}\ T_0^{\ 6})^{\ 0.2}\end{aligned} \tag{11}$$

where υ_o = 3 10^{15} Hz, T_0 = 12.2 $G_0^{\ 0.2}$ K, and τ_{100} = 0.001.

The model of dust heating used in deriving this expression assumes that the radiation incident on a grain is made up of contributions from the attenuated UV field, the 2.7 K background, and an infrared radiation field produced by dust emission at the surface of the cloud. This infrared emission is produced in a layer of thickness $A_v \sim 1$, which corresponds to an optical depth of $\tau_{100} \sim 0.001$ at 100 μm, and an equilibrium temperature T_0 =12.2 $G_0^{0.2}$ K. However, since there is thermal exchange between gas molecules and dust grains, dust temperatures derived using the previous equation should be interpreted as upper limits. High-density gas in shielded regions is usually cooler than the dust in clouds suffused with large UV radiation fields, and so will tend to cool the dust. We find that the dust temperature in the shielded regions is $T_d \sim 20$ K, which agrees well with the values inferred from the observations.

4.1.3. Heating by cosmic rays and H_2 *formation*

The cosmic ray heating term is:

$$\Gamma_{cr} \ = \ \zeta_P(H_2)\ \Delta Q_{cr}\ n(H_2)\ \ \mathrm{ergs\,cm^{-3}\,s^{-1}} \tag{12}$$

where $\zeta_P(H_2)$ is the primary cosmic ray ionisation rate of H_2, and ΔQ_{cr} is the energy deposited as heat after ionisation. Following Goldsmith & Langer (1978), values of $\zeta(H_2)$ = 2.0 $10^{-17}\ \mathrm{s^{-1}}$ and ΔQ_{cr} = 20 *eV* were adopted, leading to a total cosmic ray heating rate Γ_{cr} = 6.4 10^{-28} *n(H$_2$)* ergs $\mathrm{cm^{-3}\,s^{-1}}$.

An additional source of heating in molecular clouds is H_2 formation on grains. Some fraction of the 4.48 *eV* binding energy of the released H_2 molecule is released as kinetic energy, and transferred to the gas as heat. In a steady state, under conditions where only cosmic rays destroy H_2 molecules, and at high densities where most of the hydrogen is in molecular form, H_2 formation heating can be considered as another term in the cosmic ray heating term (see discussion in Goldsmith & Langer 1978). Accordingly, the heating rate can be expressed as:

$$\Gamma_{H_2} \ = \ \left(\frac{\Gamma_{cr}}{3}\right)\ \left(\frac{Q_{H_2}}{4.48\ eV}\right)\ \mathrm{erg\,cm^{-3}\,s^{-1}} \tag{13}$$

where Q_{H_2} is the energy released as heat. We adopt a value of Q_{H_2} = 2.0 *eV* in the work presented here.

4.1.4. CO, CI, CII, and OI line emission

The cooling due to CO, CI, and OI line emission is the same as that employed in Nelson & Langer (1997). The CO cooling

function used is an analytical fit to the cooling curves of Goldsmith & Langer (1978), and has the correct limiting behaviour in both the optically thin and optically thick limits. The cooling formulae for CII and O I were originally taken from the work of Chieze & Pineau des Forêts (1987). The cooling due to CII has been modified, however, to account for the effects of collisional de-excitation. We note that the cooling due to CII and OI dominates in the warm, photoionised outer layers of molecular clouds, but contributes little to the thermal evolution in the cooler, shielded regions in the cloud interiors. The CI emission was calculated according to the formula given in Nelson & Langer (1997), using collision rates and Einstein A coefficients taken from Genzel (1991).

One heating mechanism that has been omitted is through collisional de-excitation of IR pumped OI (63 μm) fine-structure transitions. The work of Hollenbach et al. (1991) indicates that the heating due to this process is similar to the dust heating rate, however in the case of the Eagle Nebula, simple calculations indicate that its inclusion has a negligible effect on the calculated gas temperatures.

4.2. Chemical model

The chemical model used here is the same as that used by Nelson & Langer (1997) in dynamical collapse calculations for isolated molecular clouds. This model is designed to capture the essentials of the carbon and oxygen chemistry, since these species and their molecules are responsible for the majority of the cooling that occurs in the cloud. In the model, the following species are evolved: CO, CI, CII, HCO^+, O I, He^+, H_3^+, OH_x, CH_x, M^+ and *e*. Here OH_x represents the species H_2O, OH and O_2, and CH_x represents CH_2 and CH. These species are grouped together for the sake of simplicity, and because their reactions occur at similar rates and along similar pathways. The M^+ term represents ionised Fe, Na, Mg and Ca, which provide a background source of electrons in highly shielded regions.

The chemical reactions which are evolved with time, and their associated reaction rates κ_i are listed in the Appendix.

4.3. Approach

The model that we have described is by its nature a fully time-dependent one. In developing a model for the M16 gas column, we take as a starting premise that the columns have only been exposed to the ionising radiation of the nearby O stars for the last 10^5 years. This is approximately the crossing time for the ionisation-shock front to propagate into the cloud.

Our approach to the chemical and thermal modeling has been, therefore, to evolve the chemical state of the clouds for 2 Myr, using the initial conditions described in the Appendix, and in the absence of an UV field. After this time a steady state is attained. We then use this steady state as the initial conditions for a calculation in which the UV field is switched on, and the chemical state is evolved for 10^5 years. We note that the chemical time scale is substantially shorter than this, so that the chemical profile of the cloud evolves to a steady state within this time.

Fig. 16 shows the density and temperature, and the chemical abundance profiles along a cut across the finger located 0.1 pc behind the photo-ionised outer edge of the fingertip. This computation corresponds to 10^5 years after the switch-on of the UV field. Fig. 16a) shows the density and temperature profile through the dense clump located close to the tip of the finger. We note that the temperature tends towards a value of ~ 20 K inside the dense clump, close to that estimated from the SCUBA data. This follows from the fact that the dust and gas are strongly coupled at these relatively high densities. The chemical profiles (Fig. 16b–d) are such that CO is dominant throughout the Finger, with CI and C II becoming prominent towards the edges of the cloud. The OH_x species (H_2O, O_2, and OH) are very abundant in the cloud interior.

The tip of the finger is located at $z = 0.325$ pc from the base of the model (the calculation does not attempt to model the whole finger – but just concentrates on its upper portion). The temperature is ~ 200 K at the cloud tip, and decreases rapidly to ~ 20 K in the cloud interior. The gas outside of the dense core, but deep in the cloud interior, has a slightly lower temperature because of gas-dust thermal coupling in the denser regions. Fig. 17b shows the extinction, and Figs. 17c–e show the computed chemical abundances.

The change in visual extinction moving into the cloud from its tip along the symmetry axis is plotted in Fig. 17b, and the chemical profiles are shown in Figs. 17c–e. Fig. 17c indicates that CO becomes abundant within a few A_v of the edge of the cloud, and that the between this region and the edge, carbon is primarily locked in CII and CI. The OH_x species (H_2O, O_2, and OH) are also observed to be in abundant within a few A_v of the edge the cloud. The CO profile rises more steeply than that of some other species due to CO self-shielding.

Integrating the emission from the models, we predict that the total CO emission from the finger = $6.7\,10^{31}$ ergs s^{-1} = 1/60 $L_\odot$, and the total CI emission from the finger = $2.3\,10^{30}$ ergs s^{-1} = 1 / 1700 $L_\odot$. Thus the CI cooling is therefore relatively insignificant in comparison to the situation seen elsewhere (Israel et al. 1995a, b).

5. On the nature of the condensations at the tips of the Eagle Nebula

To summarise the main observational characteristics of the clumps at the tips of the fingers; three compact, massive, dense and cold clumps have been detected close to the tips of the fingers. These clumps have no detectable compact embedded near or mid-infrared sources, radio continuum counterparts or molecular outflows. The crucial question is whether these are clumps formed by the action of a radiatively driven implosion (RDI – Lefloch & Lazareff 1994, 1995) at the finger tips, or are instead pre-existing dense cores that are either Class 0 protostars, or clumps at an earlier stage of evolution. André (1996) has proposed several criteria to define Class 0 protostars: a) they should show indirect evidence of the presence of a central YSO

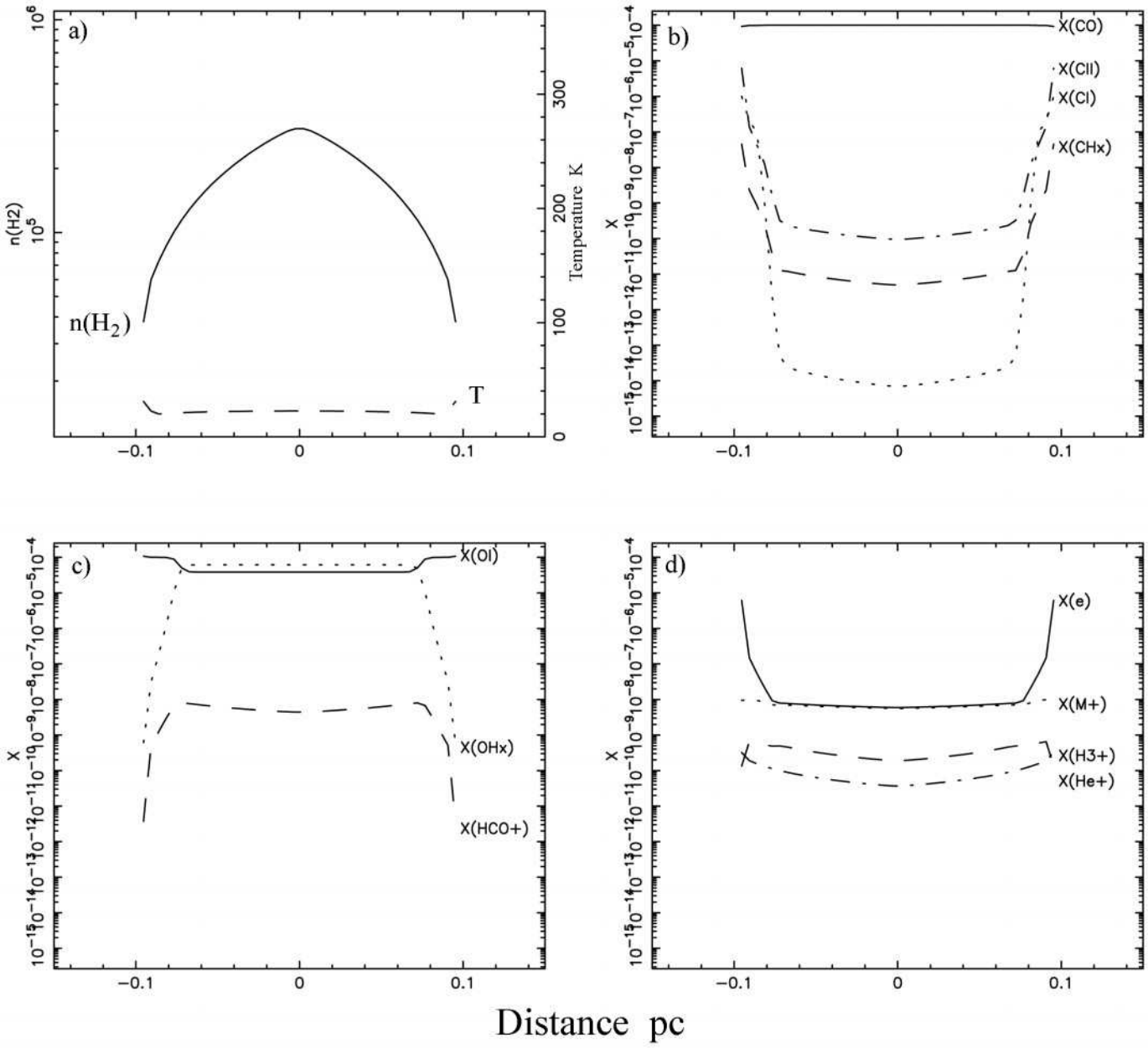

Fig. 16a–d. A cut across the modelled finger at a distance of 0.1 pc in from the photoionised edge (i.e. across the core at the tip of the finger). Panel **a** shows the adopted density and calculated temperature profiles, **b**–**d** show the computed molecular abundances 10^5 years after switching on the UV field. The column density matches that which is observed when convolved to the resolution of the J= 3–2 $C^{18}O$ data.

– for example by the detection of a compact centimetre wavelength free-free emission peak or by the presence of a collimated outflow or nearby water maser clumps, b) they should have centrally peaked but extended submillimetre continuum emission tracing the presence of a spheroidal circumstellar dust envelope, c) they should exhibit a high ratio of submillimetre to bolometric luminosity: L_{submm} / $L_{bol} >> 0.005$, where L_{submm} is the luminosity radiated longward of 350 μm (i.e. the spectral energy distribution should resemble a single temperature blackbody at $T \sim$ 15–20 K). For $\mathbf{\Pi_2}$ we estimate L_{submm} / $L_{bol} \sim 0.2$, and $L_{bol} \sim 1930\ L_\odot$. It is clear however that a) does not match the characteristics of the Eagle clumps, and that our estimates of the pressure balance between the ionisation front and the cloud interior indicate that RDI has not yet led to the compression of the finger tips (see Sect. 6). It therefore seems inescapable that they are pre-existing clumps at a very early stage of evolution. In particular no protostellar core has yet developed within the cores which could be capable of producing the UV radiation which would be needed to generate free-free radio emission. Neither has there apparently been time for a molecular outflow to develop. The other characteristics also rule out 'Class I'–'Class III' objects (see André 1996 for more detailed definitions of these categories).

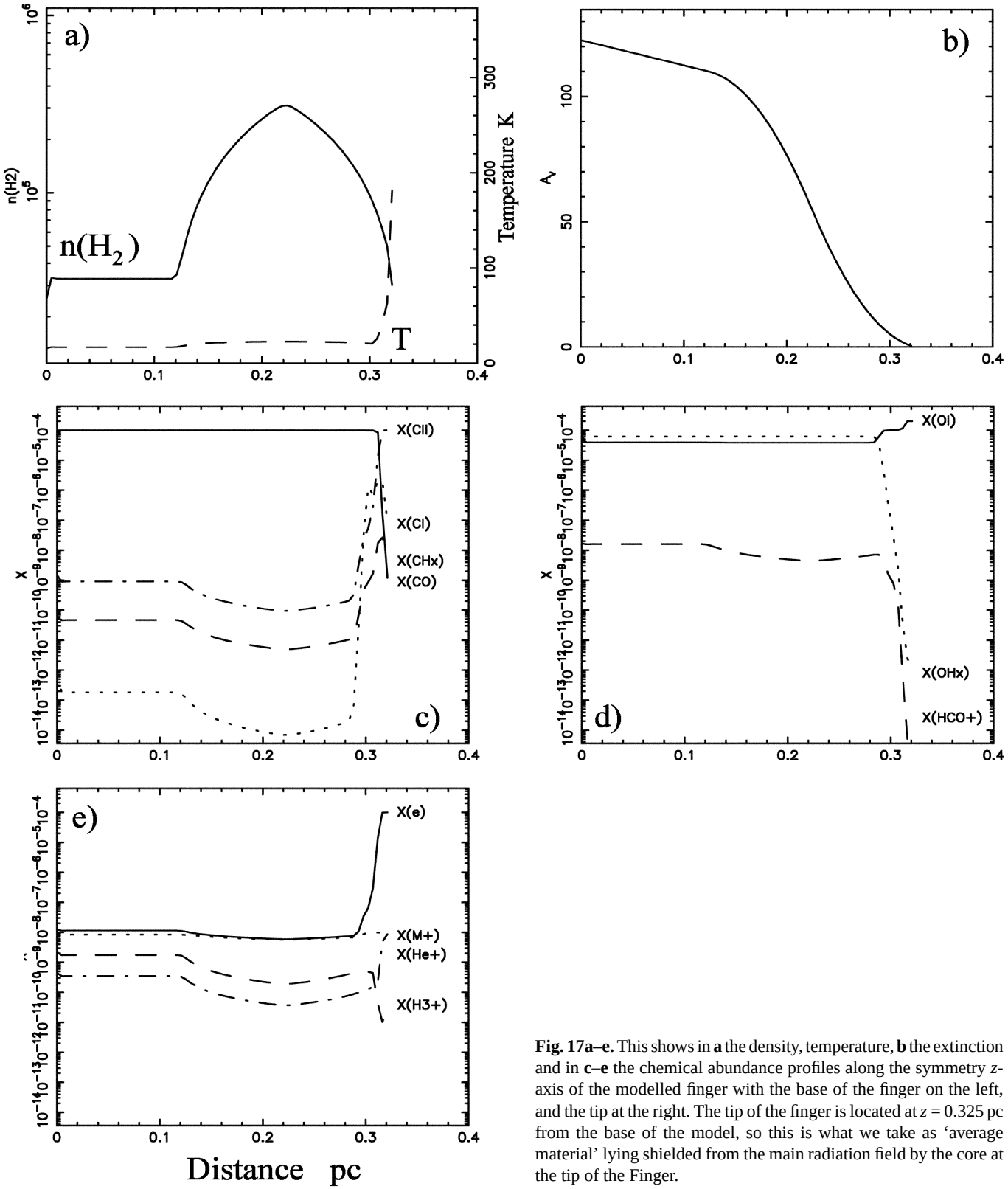

Fig. 17a–e. This shows in **a** the density, temperature, **b** the extinction and in **c–e** the chemical abundance profiles along the symmetry *z*-axis of the modelled finger with the base of the finger on the left, and the tip at the right. The tip of the finger is located at $z = 0.325$ pc from the base of the model, so this is what we take as 'average material' lying shielded from the main radiation field by the core at the tip of the Finger.

Although there have been claims of detections of almost 30 'Class 0' protostars (André 1996), there are few, if any, convincing detections of 'protostellar' objects earlier than 'Class 0'. Other, similar objects such as the protostellar condensations in NGC2024 were originally claimed by Mezger et al. (1992) to be isothermally cold (~ 20 K), massive protostars. However, subsequent IR and spectroscopic studies challenged this interpretation, following the detection of associated water maser and

molecular outflow activity (summarised in Wiesemeyer et al. 1997). Perhaps the best candidates for such an early class of objects have been the so-called 'prestellar' cores (Ward-Thompson et al. 1994, 1997). These 'starless cores' are characterised by having relatively dense cores, no outflows, and a shallow density distribution. However, it is far from clear that they are collapsing; in particular the amount of magnetic support within their cores is unknown, and the few available determinations of core temperatures are highly dependent of how much of the gas has become frozen onto, or depleted onto grains (Henriksen et al. 1997). We therefore believe that the condensations at the tips of the Eagle Nebula are amongst the best candidates so far reported as being in the earliest stage of Class 0 protostellar development.

6. Time scales and stability

One of the primary purposes of the work presented in this paper is to examine whether substantial star formation has occurred, or is likely to occur, in the fingers of the Eagle nebula. The IR observations indicate that there are no young stellar objects embedded inside the dense fingertips. This is corroborated by the relatively narrow line widths present in the molecular line observations, indicating a lack of outflow activity. By examining the time scales associated with the various physical processes acting on the clouds, we hope to create a plausible picture of their eventual fate.

The fingers are estimated to have number densities typically $n(H_2) \sim 2\ 10^4$ cm^{-3}, but in the clumps located near the tips, the density increases to $n(H_2) \sim 2\ 10^5$ cm^{-3}. For the purpose of the following discussion, we adopt a simple model for a dense clump at a fingertip which is assumed to be spherical, with a radius r = 0.085 pc, and a mass of M $\sim$ 31 M$_\odot$. We further assume that the ionising sources are located 2 pc away from the fingertip, and produces 2 10^{50} photons s^{-1}. It is observed that the peak submm continuum emission from the clumps is located $\sim$ 0.1 pc deeper into the fingers than their photoionised front surfaces.

A substantial amount of theoretical work has been carried out to try to understand the evolution of dense, gaseous clumps that are being subjected to the ionising radiation of nearby OB stars. A discussion of propagating ionisation fronts is presented in Spitzer (1968), and a number of more recent papers have been written on the subject, though with emphasis on the radiatively driven implosion (RDI) stage (Bertoldi 1989, Lefloch & Lazareff 1994, 1995), and the cometary globule stage (Bertoldi & McKee 1990).

The analysis of propagating ionisation fronts indicates that there are two distinct types, which are characterised by their propagation speed. The *R*-type ('Rarified') ionisation fronts travel through a low density medium with a velocity of $u_{IF} > 2\ c_i$, where c_i = sound speed of the ionised medium. Typically, $c_i \sim 11.4$ km s^{-1}. The second type of ionisation front is referred to as *D* -type ('Dense'), and these travel through denser gas with a velocity of $u_{IF} < (c_I^2 / 2c_i)$, where c_I = the ound speed in the pre-ionised material and $c_I << c_i$. Often a dense gaseous clump will not satisfy the conditions necessary for either an *R*-type or a *D*-type front when initially subjected to a strong ionising source. A front formed under these circumstances is called M-type, and will result in a shock being driven into the clump (RDI stage), which compresses the gas until pressure equilibrium between the ionisation front and the cloud interior is attained. Under these circumstances, the gas just ahead of the ionisation front is compressed initially by the preceding shock wave so that an approximately *D* -critical ionisation front is able to form (i.e. $u_{IF} = c_I^2/2c_i$) behind the shock front which continues to compress the cloud ahead of it. The structure of the cloud during this implosion stage, moving from the cloud surface towards its interior, consists of a hot, photoevaporating, ionised region, an approximately *D*-critical ionisation front, a dense, neutral post-shock region, a shock front, and then a pre-shocked neutral region composed of the undisturbed gas in its original state. Provided that the implosion does not induce the cloud to collapse, the post-implosion cloud then undergoes a period of slow evolution as the ionisation front slowly propagates into the cloud.

The high mass stars that provide the ionising radiation are formed within Giant Molecular Clouds (GMCs). The cloud complexes are observed to be composed of clumps, with typical densities $> 10^3$ cm^{-3}, and radii $\sim$ 1 pc, which are embedded in a warm, tenuous interclump medium (*ICM*). The ignition of an O or B star causes an *R*-type ionisation front to propagate out rapidly through the *ICM* to the Strömgren radius:

$$r_s = \left(\frac{3S}{4\pi n_i^2 \alpha_i} \right)^{\frac{1}{3}} \tag{14}$$

where n_i = particle number density of the *ICM* and α_i = the hydrogen recombination coefficient. The heating of the gas by the ionising flux leads to temperatures of $T_i \sim 10^4$ K, and sound speeds of $c_i \sim 11.4$ km s^{-1}. When the *R*-type front reaches a dense clump, it stalls and a shock is driven into the clump (RDI) until it is sufficiently compressed that a steady *D*-type ionisation front may be maintained. It is this general scenario that we have in mind when making the following numerical estimates for conditions in the fingers of the Eagle nebula.

It is necessary first of all to compare the pressure at the surface of the gas columns with that in their interior, to determine whether or not shocks are being driven into the heads of the fingers. If the pressures were approximately equal, it suggests that the fingers had already been compressed by an ionising-shock front (IS-front). Conditions in the cloud interior would allow the formation of a steady *D*-type ionisation front at the surface, which will slowly eat into the cloud. If, on the other hand, the external pressure is found to greatly exceed the internal pressure, we will interpret this to mean that an IS-front is currently being driven into the columns.

The line widths of the C^{18}O spectra are $< \Delta v >$ = 2 km s^{-1}. The pressure inside the cloud is composed of both a turbulent and a thermal contribution, so that

$$P_{int} = \sigma^2 \rho + \frac{\Re}{\mu} \rho T \tag{15}$$

where *T* is the temperature, ρ is the density, μ is the mean molecular weight, and $\Re$ is the gas constant. Assuming low temperature cores, then the thermal component of the line-width is negligible and $\sigma^2 = < \Delta v >^2 / (8\ ln\ 2)$ represents the square of the inferred turbulent velocity in the cloud. Both the observations and the thermal and chemical modelling, indicate that the temperature in the interior of the cloud is $\sim$15–20 K and the average number density $n(H_2) \sim 2\ 10^4$ cm^{-3} However the density in the clumps is estimated to be somewhat larger, with $n(H_2) \sim 2.2\ 10^5$ cm^{-3} (these values are similar to those estimated by Pound 1998). We take the upper value of the internal density to be $n(H_2) \sim 2\ 10^5$ cm^{-3}, giving an estimate for the total internal pressure of $P_{int} / k = 3.5\ 10^7$ cm^{-3} K. The thermal pressure at the tip of the $\mathbf{\Pi_2}$, estimated by Hester et al. (1996), is P_i / k = 6 10^7 cm^{-3} K, which is almost double the internal pressure. We therefore conclude that equilibrium does not exist between the cloud surface and the interior, and that an IS-front is currently propagating into the column (Megeath & Wilson 1997 find similar values for the pressure difference ($\sim$ a factor of 2) in the sample of objects they observed). We further note that the conservation conditions across a *D*-critical ionisation front predict that the pressure just ahead of the front is twice the thermal pressure just behind the front (i.e. $P_n = 2\ P_i$, where the subscripts are *n* for 'neutral' and *I* for 'ionised'. This arises because ionised material leaves the front at a velocity $v_i = c_i$.

If pressure equilibrium has in fact been attained between the ionisation front and the cloud interior, and the additional internal pressure required is provided by a magnetic field, then the field required is:

$$B = \sqrt{8\pi\,(P_{ext} - P_{int})} = 5.4 \quad 10^{-4}\ \mathrm{G} \tag{16}$$

Work presented by Myers & Goodman (1988) indicates that there is usually an approximate equipartition between the magnetic and kinetic energies in molecular clouds, so that the turbulent line widths should be Alfvénic. If a magnetic field is responsible for providing an internal pressure inside the fingers which is capable of balancing the pressure at the ionisation font, then it is apparent that equipartition does not hold, since the Alfvén speed corresponding to a field of 5.4 10^{-4} G is v_A = 1.9 km s^{-1}. Alfvénic motions would then lead to an observational linewidth of:

$$\langle \Delta v \rangle = \sqrt{8 \ln 2 v_A^2} = 4.4\ \mathrm{km\ s^{-1}} \tag{17}$$

which is about twice as large as that observed from the C^{18}O lines which trace the material in the core.

The pressure of the large scale magnetic field is anisotropic, and provides a stress that is in a direction perpendicular to the field direction. Alfvén waves, on the other hand, are able to provide an isotropic pressure, which is given by:

$$P_\omega = \frac{\delta B^2}{8\pi} \tag{18}$$

where δB is the perturbation to the mean magnetic field associated with the Alfvén wave. The fluid velocity perturbation associated with this travelling wave is (from McKee & Zweibel 1995):

$$\delta v = \frac{\delta B}{\sqrt{4\pi\rho}} \tag{19}$$

We therefore have the relation:

$$\frac{\delta \nu}{\nu_A} = \frac{\delta B}{B} \tag{20}$$

where *B* is the mean magnetic field strength, and v_A is the Alfvén speed associated with the mean field. For $\delta v << v_A$, the mean field dominates over the random field component, and internal stresses provided by the magnetic field are strongly anisotropic. If this were the case in the Eagle nebula, then the morphology of the fingers should reflect this internal, anisotropic pressure. The observations of the fingers, and of $\mathbf{\Pi}_2$ in particular, indicate a substantial degree of cylindrical symmetry. The direction of elongation of the fingers points towards the ionising sources, and is therefore most probably caused by the ionising radiation rather than by an ordered magnetic field. We therefore conclude that a large-scale ordered magnetic field does not produce an internal pressure that can balance the pressure of the ionisation front. A magnetic field in which the disordered component was comparable to the ordered component would yield internal motions $\sim \nu_A$ since:

$$\frac{\delta B}{B} = \frac{\delta v}{\nu_A} \ \cong\ 1 \tag{21}$$

This equipartition of kinetic and magnetic energy is observed in numerical simulations of MHD turbulence (e.g. Gammie & Ostriker 1996). As described above, these motions would lead to linewidths $< \nu > \sim 4.4$ km s^{-1}, which are not seen in the data. We conclude that there is insufficient internal pressure in the fingers of the Eagle nebula to balance the pressure at the ionisation front, and that an ionisation-shock front is currently being driven into the cloud.

The presence of a shock front currently propagating into the columns indicates that the dense clumps located towards their tips are probably not the result of radiatively driven implosion. When an IS-shock front propagates into a cloud, the shock front precedes the ionisation front (located at the optical surface of the cloud) by a small distance. This would preclude it from traversing the top $r \sim 0.2$ pc of $\mathbf{\Pi_2}$, and forming the clump there. Instead, it seems likely that the dense clumps located towards the tips of the fingers are part of a larger, dense structure that pre-existed the expansion of the HII region, but have now come into stark contrast with their local environment due to the photoionisation of the surrounding, lower density material. The pre-existence of this dense structure, and its associated shadowing effect, have probably contributed to the formation and appearance of the pillars, and the fact that they point towards the external O-stars.

The shock propagation velocity may be derived from the usual shock discontinuity jump conditions, leading to the equation

$$V_s^2 = \frac{(P_{sn} - P_n)}{\rho_n} \left(1 - \frac{\rho_n}{\rho_{sn}}\right)^{-1} \tag{22}$$

where P_{sn} and ρ_{sn} are the pressure and density of the shocked, neutral material and P_n and ρ_n are the pressure and density of the pre-shocked neutral material. We have no direct knowledge of what to expect for ρ_{sn}, since we only know the pressure and do not have an independent estimate of the density and sound speed in this region. If we assume that $2 \leq \rho_{sn}/\rho_n \leq \infty$ then the previous equation may be expressed as:

$$V_s^2 = \alpha \frac{(P_{sn} - P_n)}{\rho_n} \tag{23}$$

where $1 < \alpha < 2$, so that the maximum error that we incur in our estimate of V_s, as a result of guessing the value of ρ_{sn}, is a factor of $\sqrt{2}$. We take P_{sn} = 2P_i and ρ_n = 2 10^5 $m(H_2)$, where $m(H_2)$ is the mass of a hydrogen molecule, which then leads to a shock velocity of $V_s \approx 1.3\,\mathrm{km\,s^{-1}}$. The time-scale for this shock to propagate through the top 0.2 pc of the finger tip is then τ_{sh} = 0.2 pc / $V_s \approx 1.5\ 10^5$ years, which is comparable to shock crossing times derived by Bertoldi (1989) for the dense clumps located in the Rosette nebula that appear to be undergoing implosion.

These shock crossing times are considerably shorter that the estimated ages of the O-stars in the Rosette and Eagle nebula (i.e. ~ 1 Myr), indicating that the structures being observed now (cometary globules or elephant trunks) have only been exposed to the ionising radiation of the nearby stars for a relatively short time. An upper limit for the time taken for an R-type ionisation front to reach the elephant trunks during the initial expansion of the Strömgren sphere is given by τ_R = (2 pc / 2 c_i) = 8.8 10^4 years (i.e. a relatively short time after the switch-on of the O stars). The implication of this rapid time for the initial expansion of the HII region is that previously there must have been intervening dense structures shielding the pillars from the ionising flux of the stars, which have only recently been eroded away, exposing the pillars to the UV radiation.

7. The future evolution of the fingertip cores

We may now ask what the eventual fate of the dense clumps in the fingers is likely to be. Using the virial theorem, assuming a constant density profile for the clumps, and assuming them to be immersed in a background medium which exerts a surface pressure P_s, we obtain for the virial mass:

$$M_v = \frac{5r}{6G}\left(\sigma^2 + \frac{3\Re T}{\mu}\right) \times \sqrt{\left(\sigma^2 + \frac{3\Re T}{\mu}\right)^2 - \frac{48Gr^2P_s}{5}} \tag{24}$$

where r is the clump radius, and G is the gravitational constant (Bowers & Deeming 1984). If the clumps are immersed in background material of number density $n(H_2)$ = 2 10^4 cm^{-3}, the line widths inside and outside the clump are $\sim 2\,\mathrm{km\,s^{-1}}$, and the clumps have a radius of r = 0.083 pc, then the estimated virial mass is M_v = 21.6 $M_\odot$, The clump mass consistent with the submm dust emission is M $\sim$20 $M_\odot$, and that estimated from the CO column density is M $\sim$30 $M_\odot$, indicating that the core of $\mathbf{\Pi_2}$ is either marginally stable against collapse, or in the earliest stages of Class 0 development. The similarity of the clump and virial masses adds weight to the argument that all of the clumps pre-existed the exposure of the fingers to the ionising radiation of the stars. It is likely that they are gravitationally bound objects, and not density enhancements resulting from a radiation driven implosion.

When the IS-front propagates into the clumps, the effective external pressure acting on the clumps will rise from P / k = 3.5 10^6–1.2 10^8 cm^{-3} K, resulting in the cloud being strongly compressed. The question of whether this shock-induced implosion will lead to star formation in the clumps, or to their disruption, remains unclear, since the crossing time of the shock and the gravitational free-fall time of the clump are comparable (i.e. $\tau_{sh} \sim \tau_{ff} \sim 10^5$ years). It is likely that numerical simulations will be required to provide a definitive answer to both this question, and to develop an understanding of the relationship of the prodigious star formation rate in the EGG′s to that of the fingers.

Although we have concluded that the dense clumps observed in the fingertips have not been formed by the action of RDI, we note that the clumps have an elongated appearance as seen in Fig. 4. This is probably due to the pressure of the IS-front beginning to compress the clumps as the front propagates into the fingers.

8. Conclusions

1. Molecular line, millimetre/submillimetre/radio continuum, and mid-IR observations are reported of the opaque fingers which cross the Eagle Nebula. These are examined, along with optical and near-IR data to measure the physical environment within the fingers, and to examine their potential for being future sites of star-formation.
2. The fingers are surprisingly warm when viewed in the CO J= 3–2 lines, with peak temperatures approaching 60 K. The lines are however relatively narrow, and there is no compelling evidence for any molecular outflow activity. The masses of the fingertip cores determined from CO isotopomeric observations range from $\sim$ 10 to 60 $M_\odot$, and they contain 55–80% of the total mass of each of the fingers. The total mass contained in the three fingers and the nearby extended material is $\sim$ 200 $M_\odot$.
3. The velocity fields of the gas are complex and show that the material is very clumpy. The best evidence for coherent velocity structure is along the centre finger, where a velocity gradient $\sim 1.7\,\mathrm{km\,s^{-1}\,pc^{-1}}$ is seen. There may be evidence for somewhat larger velocity gradients, however these are difficult to untangle from the clumpy structure of the gas.
4. The fingers contain a number of embedded submm continuum cores. The most intense cores in each finger are found close to the tips of the fingers. The continuum spectra of these cores suggest that they are much cooler, $\sim$ 20 K, than the gas temperatures measured by the CO observations.
5. Detailed modelling shows that the fingers should contain dense cold cores surrounded by a sheath of warm molecular

gas. These characteristics prove to be an excellent match to the observational data.

6. The radio and morphological evidence suggest that the UV radiation field incident on the surfaces of the fingers is $\sim 1700\ G_o$.
7. A simple thermal and chemical model of a finger structure was developed to study their internal physical environment. This model suggests that the fingers should contain cold (~ 20 K) dense cores near their tips, surrounded by a sheath of warm (> 100 K) gas. The model predictions are consistent with all of the available observations.
8. The fingers appear to have been formed after primordial dense clumps in the original cloud (which formed NGC 6611) were irradiated by the light of its own OB stars. These primordial clumps have shielded material behind it from the photoevaporative dispersal of the cloud, leading to the formation of the finger structures. The cores appear to be at a very early stage of pre-protostellar development: there are no embedded infrared sources or molecular outflows present. The pressure inside the cores appears to be just less than that of the surrounding gas, and the consequence is that the material in the cores is being compressed by the external medium. It is well known that such characteristics are those shared by the earliest stages of objects popularly known as 'protostars'. *The cores in the tips of the Eagle Nebula's fingers appear to have the characteristics which are expected for objects in the very earliest stages of (pre-) protostellar activity*.

Acknowledgements. We gratefully acknowledge the contributions made by several colleagues at various stages during the evolution of this paper; in particular we thank Gene Capriotti for making some calculations to examine the importance of Rayleigh-Taylor instabilities, Mike Luhman for advice on estimating G_o, John Dyson and Tom Hartquist for discussions about cloud stability and shocks, Tom Bania for use of his archival VLA data, Bill Langer for discussions on chemical modelling, Sylvain Bontemps for discussions about protostellar collapse, and Marc Pound for discussions on the mass derivations reported in his paper of BIMA observations of the Eagle Nebula. GW thanks the Director and staff of Stockholm Observatory, for the friendly and stimulating atmosphere and use of facilities where some of the analysis was carried out. The National Radio Astronomy Observatory is operated by Associated Universities Inc., under co-operative agreement with the National Science Foundation. The JCMT is managed by the Joint Astronomy Centre in Hilo, Hawaii on behalf of the Particle Physics & Astronomy Research Council (United Kingdom), the National Research Council (Canada), and the Nederlandse Organisatie voor Wetenschappelijk Onderzoek (The Netherlands).

Appendix A: chemical reactions used in the modelling

A.1. Cosmic ray ionisation (units $\mathrm{s^{-1}\ mol^{-1}}$)

$$cr + H_2 \rightarrow H_3^+ + e + H + cr \quad k_1 = 1.2\ 10^{-17} \tag{A1}$$

$$cr + He \rightarrow He^+ + e + cr \quad k_2 = 6.8\ 10^{-18} \tag{A2}$$

A.2. Ion-molecule reactions (units $\mathrm{cm^3\ s^{-1}\ mol^{-1}}$)

$$H_3^+ + CI \rightarrow CH_x + H_2 \quad k_{10} = 2\ 10^{-9} \tag{A3}$$

$$H_3^+ + OI \rightarrow OH_x + H_2 \quad k_{11} = 8\ 10^{-10} \tag{A4}$$

$$H_3^+ + CO \rightarrow HCO^+ + H_2 \quad k_{12} = 1.7\ 10^{-9} \tag{A5}$$

$$He^+ + H_2 \rightarrow He + H + H^+ \quad k_{13} = 7\ 10^{-15} \tag{A6}$$

$$He^+ + CO \rightarrow C^+ + O + He \quad k_{14} = 1.6\ 10^{-9} \tag{A7}$$

$$C^+ + H_2 \rightarrow CH_x + H \quad k_{15} = 4\ 10^{-16} \tag{A8}$$

A.3. Neutral-neutral reactions (units $\mathrm{cm^3\ s^{-1}\ mol^{-1}}$)

$$OI + CH_x \rightarrow CO + H \quad k_{100} = 2\ 10^{-10} \tag{A9}$$

$$CI + OH_x \rightarrow CO + H \quad k_{101} = 5.8\ 10^{-12}\ T^{0.5} \tag{A10}$$

A.4. Electron recombination (units $\mathrm{cm^3\ s^{-1}\ mol^{-1}}$)

$$He^+ + e \rightarrow He + h\nu \quad k_{200} = 9\ 10^{-11}\ T^{-0.64} \tag{A11}$$

$$H_3^+ + e \rightarrow H + H_2 \quad k_{201} = 1.9\ 10^{-6}\ T^{-0.54} \tag{A12}$$

$$C^+ + e \rightarrow CI + h\nu \quad k_{202} = 1.4\ 10^{-10}\ T^{-0.61} \tag{A13}$$

$$HCO^+ + e \rightarrow CO + H \quad k_{203} = 3.3\ 10^{-5}\ T^{-1.0} \tag{A14}$$

$$M^+ + e \rightarrow M + h\nu \quad k_{204} = 3.8\ 10^{-10}\ T^{-0.65} \tag{A15}$$

A.5. Photoreactions (units $\mathrm{s^{-1}\ mol^{-1}}$)

$$h\nu + CI \rightarrow C^+ + e \quad G_{400} = 3\ 10^{-10}\ G_o\ e^{-3A_\nu} \tag{A16}$$

$$h\nu + CH_x \rightarrow CI + H \quad G_{401} = 1\ 10^{-9}\ G_o\ e^{-1.5A_\nu} \tag{A17}$$

$$h\nu + CO \rightarrow CI + O \quad G_{402} = 1\ 10^{-10}\ \chi\ G_o\ e^{-3A_\nu} \tag{A18}$$

where χ is the CO self-shielding factor

$$h\nu + OH_x \rightarrow OI + H \quad G_{403} = 5\ 10^{-10}\ G_o\ e^{-1.7A_\nu} \tag{A19}$$

$$h\nu + M \rightarrow M^+ + e \quad G_{404} = 2\ 10^{-10}\ G_o\ e^{-1.9A_\nu} \tag{A20}$$

$$h\nu + HCO^+ \rightarrow CO + H \quad G_{405} = 1.5\ 10^{-10}\ G_o\ e^{-2.5A_\nu} \tag{A21}$$

A.6. Charge transfer reactions (unit $\mathrm{cm^3\ s^{-1}\ mol^{-1}}$)

$$H_3^+ + M \rightarrow M^+ + e + H_2 \quad k_{501} = 2\ 10^{-9} \tag{A22}$$

Appendix B: conservation conditions

Along with the above sets of reactions, we also use the following conservation conditions when evolving the chemistry

$$n(e) = n(C^+) + n(He^+) + n(H_3^+) = n(M^+) \tag{B1}$$

$$n(He_{total}) = n(He) + n(He^+) \quad \text{(B2)}$$

$$n(M_{total}) = n(M) + n(M^+) \quad \text{(B3)}$$

The following fractional abundances are assumed for our models:

$$n(C_{total}) = 10^{-4}\ n(H_2) \quad \text{(B4)}$$

$$n(O_{total}) = 2\ 10^{-4}\ n(H_2) \quad \text{(B5)}$$

$$n(He_{total}) = 0.28\ n(H_2) \quad \text{(B6)}$$

$$n(M_{total}) = 10^{-7}\ n(H_2) \quad \text{(B7)}$$

Appendix C: initial conditions

When evolving the time-dependent chemistry, we use the following initial conditions:

$$n(CI) = n(CO) = n(CH_x) = n(HCO^+) = 0 \quad \text{(C1)}$$

$$n(C^+) = n(C_{total}) \quad \text{(C2)}$$

$$n(OI) = n(O_{total}) \quad \text{(C3)}$$

$$n(M^+) = n(M_{total}) \quad \text{(C4)}$$

$$n(He^+) = \frac{k_1}{k_{200}n(e) + k_{13}n(H_2)} n(He_{total}) \quad \text{(C5)}$$

$$n(H_3^+) = \frac{k_1}{k_{201}n(e) + k_{11}n(OI)} n(H_2) \quad \text{(C6)}$$

$$n(e) = n(C^+) + n(He^+) + n(M^+) \quad \text{(C7)}$$

References

André P., 1996, Mem S.A.It 67, 901
André P., Montmerle T., 1994, ApJ 420, 837
André P., Ward-Thompson D., Motte F., 1996, A&A 314, 625
Balser D.S., Bania T.M., Rood R.T., Wilson T.L., 1995 ApJS 100, 371
Beckwith S.V.W., Sargent A.I., 1991, ApJ 381, 250
Bertoldi F., 1989, ApJ 346, 735
Bertoldi F., McKee C.F., 1990, ApJ 354, 529
Bowers R., Deeming T., 1984, Astrophysics II – The Interstellar Medium. Jones & Bartlett Publishers, 410
Chandler C.J., Koerner D.W., Sargent A.I., Wood D.O.S., 1995, ApJ 449, L139
Chieze J-P., Pineau des Forêts G., 1987, A&A 183, 98
Eiroa C., Palacios J., Casali M.M., 1998, A&A, in press
Gammie G.F., Ostriker E.C., 1996, ApJ 466, 814
Genzel R., 1991, Physical conditions and heating/cooling processes in high mass star formation regions. In: Mouschovias T., Lada C.J. (eds.) Physics of Star Formation and Early Stellar Evolution, Kluwer Press
Gibb A.G., Little L.T., 1998, MNRAS 295, 299
Goldsmith P.F., Langer W.D., 1978, ApJ 222, 881
Habing H.J,. 1968, Bulletin Astr. Inst. Netherlands 19, 421
Henriksen R., André P., Bontemps, S., 1997, A&A 323, 549
Hester J., Scowen P.A., Sankrit R., et al., 1996, AJ 111, 2349
Hillenbrand L.A., Massey P., Strom S.E., Merrill K.M., 1993, AJ 1906, 106
Hogerheijde M., 1998, Ph.D. Thesis, University of Leiden
Hollenbach D.J., Tielens A.G.G.M., Takahashi T., 1991, ApJ 377, 192
IPAC, 1997, http://crystal.ipac.caltech.edu:8001/applications/IGA/
Israel F.P., White G.J., Baas F., 1995a, A&A 302, 343
Israel F.P., White G.J., Baas F., 1995b, A&A 317, 299
Keene J., 1987, Proc. SETI Conference "Carbon in the Galaxy"
Kurucz R.L., 1979, ApJS 40, 1
Launhardt R., Ward-Thompson D., Henning Th., 1997, MNRAS 288, L45
Lefloch B. Lazareff B., 1994, A&A 289, 559
Lefloch B. Lazareff B., 1995, A&A 301, 552
Lefloch B. Lazareff B., Castets A., 1997, A&A 324, 249
Mathis J.S., Whiffen G., 1989, ApJ 341, 808
McCaughrean M.J., 1997, In: Reipurth B., Bertout C. (eds.) Proc IAU Symposium 182, Herbig-Haro Flows and the Birth of Low-Mass Star. Kluwer Press, p. 551.
McKee C.J., Zweibel E., 1995, ApJ 440, 686
Megeath S.T., Wilson T.L. 1997, AJ 114, 1106
Mezger P.G., Chini R., Kreysa E., Wink J.E., Salter C.J., 1988, A&A 191, 44
Mezger P.G., Sievers A.W., Haslam C.G., et al., 1992, A&A 256, 631
Minchin N., White G.J., Ward-Thompson D., 1995, A&A 302, L25
Mufson S.L., Fountain W.F., Gary G.A., et al., 1981, ApJ 248, 992
Myers P., Goodman A.A., 1988, ApJ 329, 392
Nelson R.P., Langer W., 1997, ApJ 482, 796
Oort J.H., Spitzer L., 1955, ApJ 121, 6
Pilbratt G.L., Altieri B., Blommaert J.A.D.L., et al., 1998, A&A 333, L9
Pound M.W., 1998, ApJ 493, L113
Spitzer L. Jr., 1968, Diffuse Matter in Space. Interscience, New York
Schneps M.H., Ho P.T.P., Barrett A.H., 1980, ApJ 240, 84
Tucholke H-J., Geffert, M., Thé P.S., 1986, A&AS 66, 311
Ward-Thompson D., André P., Scott P.F., Hills R.E., 1994, MNRAS 268, 276
Ward-Thompson D., Chini R., Krugel E., André P., Bontemps S., 1995, MNRAS 274, 1219
Ward-Thompson D., André P., Scott P.F., Hills R.E., 1997, In: Malbet F., Castets A. (eds.) Proc IAU Symp 182, Low Mass Star Formation – from Infall to Outflow. p 257
White G.J., Padman R., 1991, Nat 354, 511
White G.J., Sandell G., 1995, A&A 299, 179
White G.J., Casali M., Eiroa C., 1995, A&A 298, 594
White G.J., Lefloch B., Fridlund C.V.M., et al., 1997, A&A 323, 931
Wiesemeyer H., Güsten R., Wink J.E., Yorke H.W., 1997, A&A 320, 287